공학박사 학위논문

Defect engineering of graphene and MoS_2: First-principles calculations of structural and electronic properties

그래핀과 이황화몰리브덴의 결함 공학:

구조적 및 전자적 성질에 대한 제일원리계산 연구

2019년 8월

서울대학교 대학원

재료공학부

이 성 우

Abstract

Defect engineering of graphene and MoS_2: First-principles calculations of structural and electronic properties

Sungwoo Lee

Department of Materials Science and Engineering

The Graduate School

Seoul National University

In 2004, graphene was first synthesized and started to attract lot of attention because of its outstanding properties and physical phenomena that were not found in conventional materials. From this, a new field of 2D materials research has been opened. In addition to graphene, various 2D materials such as transition metal dichalcogenides, hexagonal boron nitride, and phosphorene were being predicted and synthesized. The applications, such as transparent electrodes, transistors, photo-detectors, batteries, filters and biotechnology, are as diverse as the various types of 2D materials. However, there is a barrier of single-crystal/large-area synthesis to replace the conventional materials by 2D materials. Defects created during synthesis of 2D materials reduce the superior properties of the 2D materials and weaken their value for applications. However, research has also been reported to improve the properties of 2D materials or to manifest unprecedented characteristics or phenomena. These studies are collectively referred to as *defect engineering* of 2D materials. In this dissertation, we study the structural and electronic properties of

defects in graphene and MoS_2 using first-principles calculations.

First, we investigated how the interaction of Fe atom pairs in graphene changes with deformation of graphene. When Fe atoms are covalently bonded to adjacent two vacancies of graphene, the interaction between two Fe atoms exhibits magnetic moment of 2 μ_B. However, we found that when stretching or compressively outward bending was applied, interaction between Fe atoms was changed and magnetic moment was vanished dramatically. In this process, it was confirmed that the adjacent carbon atoms hindered interaction between Fe atoms, and the electronic structure analysis was performed to explain our results.

Second, stability and electronic properties of Cr and V substitutional dopants in monolayer MoS_2 were investigated. We considered the charge states of Cr and V, and possible binary phases of Cr-S and V-S in order to describe the experimental situation when Cr and V dopants are formed. We confirmed that Cr_{Mo} is electrically neutral and V_{Mo} is stable in −1 and neutral state, and V_{Mo} in neutral state has a local magnetic moment of 1 μ_B.

Third, we studied atomic-scale mechanism of the structural phase transition due to the formation of S vacancies in triangular MoS_2 nanocrystals. Reaction barrier energy calculations were performed to explain recent experimental results of changing the 2H phase to 1T phase by CO gas annealing. The reaction barrier energy calculations confirmed that the S atoms at the vertex and edge of the nanocrystals can be easily desorbed by CO molecules. Then, local structure changed to 1T phase when S atoms at basal plane migrate to the space around S vacancy. As a result, we could suggest novel atomic-scale mechanism of structural phase transition which is consisted of S vacancy formation and S atom migration.

Through these studies, we were able to understand detailed structural and electronic properties of defects in graphene and MoS_2. In addition, the results presented in this dissertation are expected to be a guideline for the development of novel nanodevices and catalysts through defect engineering of 2D materials.

Keywords: 2D materials, Graphene, MoS_2, Defect, Density functional theory, First-principles calculations

Student Number: 2014-30212

Table of Contents

List of tables

List of figures

Chapter 1. Introduction

1.1. Emergence of 2D materials research

The possibility of synthesis of graphene has been predicted for decades already [1–3]. However, experimentally, it has been difficult to synthesize or separate graphene from graphite. Surprisingly, in 2004, A. K. Geim and K. S. Novoselov first separated graphene by a very simple method using Scotch tape (Figure 1.1) [4]. This has attracted a lot of interest from the scientific and technological community. A. K. Geim and K. S. Novoselov, who first separated graphene, published important research results on graphene since 2004 [4–6]. Since then, research on graphene has started to increase explosively and last year more than 30,000 papers were published (Figure 1.2.a). Recognized for this influence, A. K. Geim and K. S. Novoselov won the Nobel Prize for Physics in 2010 (Figure 1.2.b), just six years after the first separation of graphene. This is an example of the discovery of graphene has had a profound impact on science and technology.

Since then, there has been a new field of two-dimensional (2D) material research. Other two-dimensional materials besides graphene have been newly predicted and synthesized. Transition metal dichalcogenides (TMD) [7–12], hexagonal boron nitride (h-BN) [13–19], and phosphorene [20–25] are representative 2D materials (Figure 1.3).

TMD, which is a combination of a transition metal and a chalcogen element, exhibit semiconducting or metallic character according to its composition and structure. Researchers are trying to use TMD mainly as optoelectronic applications [11,26,27], and more recently, there are many studies on the characteristics as catalyst [7,28–30].

h-BN is an insulator with a band gap of about 5.2 eV and is excellent in thermal/chemical stability. It is widely used as an insulating or encapsulation layer

Figure 1.1. (Upper panel) Atomic model for hexagonal structure of graphene. Images from https://energymetalnews.com/2018/11/14/graphene-stocks-to-benefit-from-new-applications-in-lithium-ion-batteries. (Lower panel) A lump of graphite, a graphene transistor, and a tape dispenser. Donated to the Nobel Museum in Stockholm by A. K. Geim and K. S. Novoselov in 2010. Photo courtesy of Gabriel Hildebrand.

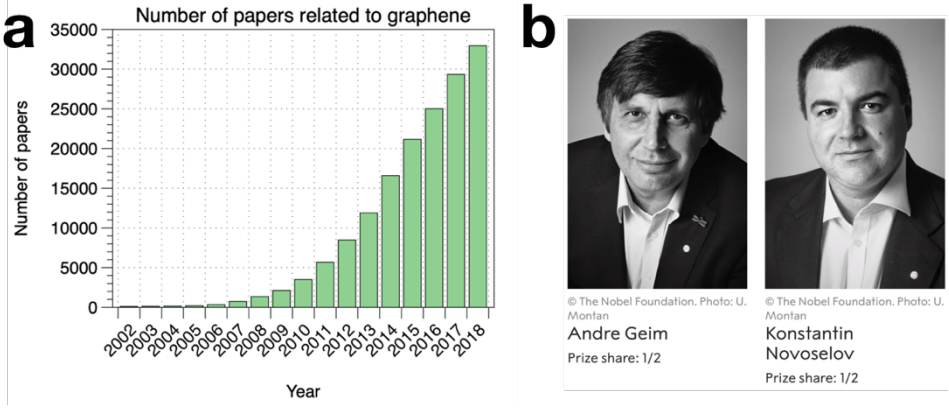

Figure 1.2. a) A graph showing that the number of papers related to graphene increases annually. b) A. K. Geim and K. S. Novoselov, who laureates of Nobel Prize in Physics, 2010. Photo courtesy of the Nobel Foundation.

for electronic devices based on 2D materials [15,31,32].

Phosphorene, also called black phosphorus, is a novel 2D material consisting only of phosphorus and has a somewhat peculiar shape. Phosphorene monolayer is a semiconductor material with a band gap of about 1.6 to 2.0 eV. There are also attempts to utilize phosphorene for various applications.

In addition, various 2D materials such as layered metal oxide (LMO) [33–35], borophene [36,37], germanene [38–40], and etc. have been continuously discovered, and research on these 2D materials is actively carried out. There are as many applications as there are different kinds of 2D materials. As shown in Figure 1.4, there are broad applications such as transparent electrodes [41,42], transistors [4,43,44], photodetectors [11,35,45,46], batteries [47,48], filters [49], and biotechnology [50,51].

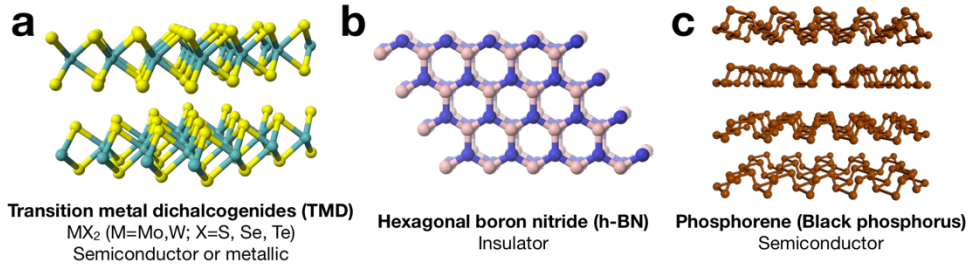

Figure 1.3. Representative 2D materials. Atomic model of a) TMD, b) h-BN, and c) phosphorene.

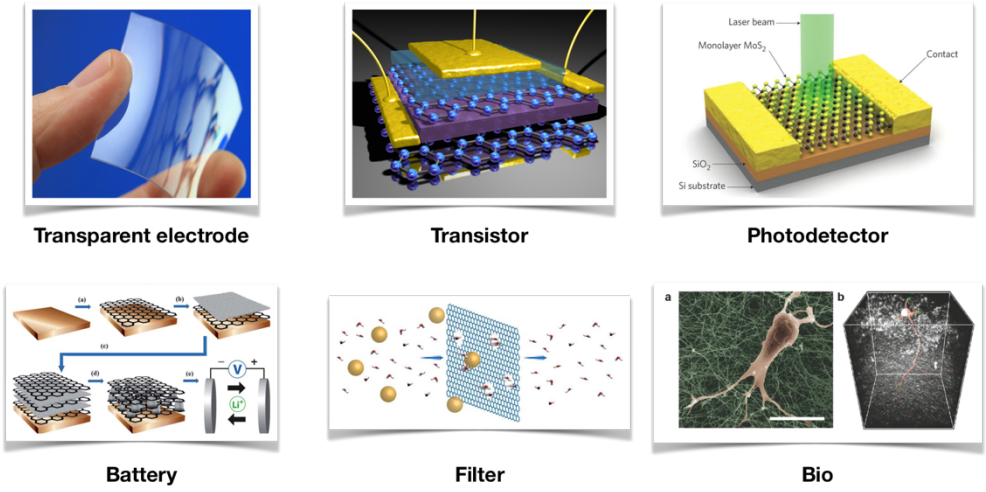

Figure 1.4. Various applications of 2D materials. Image sources are http://www.enews.tech/graphene-computer.html, https://physicsworld.com/a/vertical-graphene-transistor-avoids-leakage, [52], [53], [49], and [54] from top left to bottom right. Last four images are reprinted with permission. Copyright 2013 Springer Nature, 2011 RSC Publishing, and 2017 John Wiley & Sons for [52], [53], and [54], respectively.

1.2. Defects in 2D materials and its negative effects

Despite the diversity of 2D materials and the existence of their outstanding and unusual properties, replacing existing materials has many problems. The main reason for this is that it is difficult to synthesize 2D materials as a large-area single crystal without defects.

One example is the difference between theory and reality of graphene's mobility. Theoretical limit of carrier mobility of graphene was predicted as ~ 200,000 $cm^2/(V \cdot s)$ at room temperature [55]. However, mobility of graphene depends on the crystallinity and the surrounding environments. Table 1.1 shows experimental result on graphene's mobility showing large variation. It can be seen that the sample obtained through mechanical exfoliation exhibits generally higher mobility than the sample synthesized by CVD. Depending on the device structure, there is also a significant variation in mobility. All of these results are below the theoretical limits.

One of the main reasons for the discrepancy between theory and experiment is defects. J. -Y. Hwang *et al.* reported a correlation between carrier mobility and defect density in large-scaled graphene films prepared CVD method [56]. They controlled growth condition for the graphene sample to control defect density of the sample. They used Raman spectroscopy to identify layer number and crystal quality of the sample and estimated defect density. Figure 1.5 shows correlation between experimentally estimated defect density and carrier mobility. Fitting data on samples clearly shows a tendency for carrier mobility decreases as the defect density increases.

Theoretical study on this subject was also carried out. A. Betti *et al.* performed atomistic simulations on the mechanism of carrier scattering in graphene nanoribbon (GNR) [57]. They performed TCAD simulation to solve Poisson equation and Schrödinger equation using non-equilibrium Green's function formalism. Defect-limited mobility in various conditions is plotted in Figure 1.6. In Figure 1.6.a and

Table 1.1. Summary of studies related to graphene's mobility.

Year	Reference	Synthesis method	Sample size	Device structure	Mobility
2009	F Chen *et al.* [58]	Mechanical exfoliation	< 10 μm	Dielectric/Gr/SiO_2	~ 70,000
2010	JY Hwang *et al.* [56]	CVD	~ cm	Gr/SiO_2/Si	~ 1350
2011	A S Mayorov *et al.* [59]	Mechanical exfoliation	~ mm	h-BN/Gr/h-BN	~ 100,000
2012	C Lu *et al.* [60]	CVD	~ μm	Gr/PET	< 8,000
2015	L Banszerus *et al.* [32]	CVD	~ 10 μm	h-BN/Gr/h-BN	~ 50,000

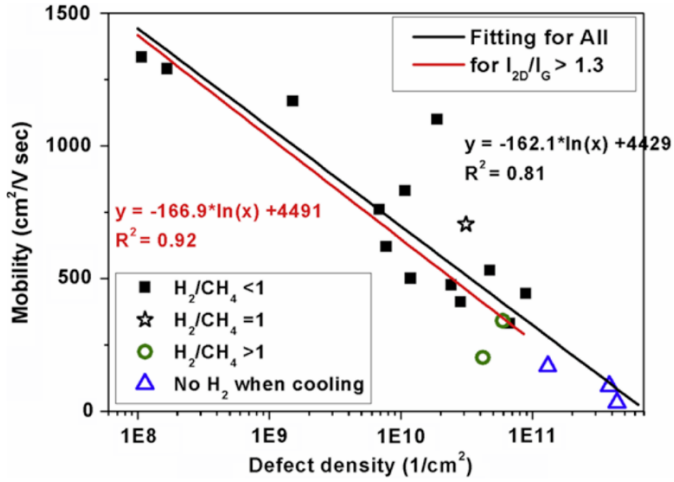

Figure 1.5. The carrier mobility of graphene samples corresponding to their calculated defect density. The black square, black hollow star and green hollow circle represent H_2/CH_4 ratio less than, equal to and larger than 1, respectively; the blue hollow triangle specifies samples prepared without H_2 incorporation at the cooling stage. The black line shows a logarithmic fitting of all data points and the red line is a fitting result based on those samples showing $I_{2D}/I_G > 1.3$ (monolayer dominant). Reprinted with permission from [56]. Copyright 2010 IOP Publishing.

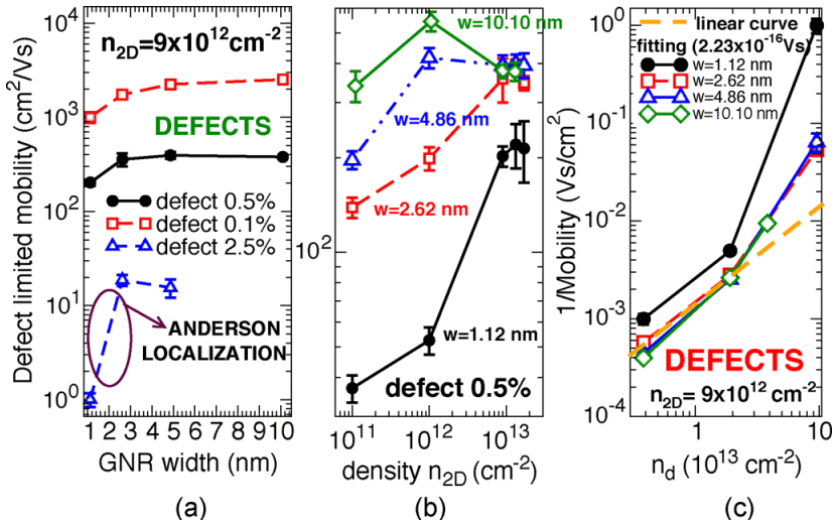

Figure 1.6. a) Defect-limited mobility as a function of W for $n_{2D} = 9 \times 10^{12}$ cm^{-2} and for different defect fractions n_d. b) Mobility as a function of n_{2D} for a defect fraction $n_d = 0.5\%$. c) Inverse of the mobility as a function of n_d for $n_{2D} = 9 \times 10^{12}$ cm^{-2} and for different GNR widths W. Reprinted with permission from. Copyright 2011 IEEE.

1.6.c, It can be seen that carrier mobility decreases with increasing defect density regardless of width *W* of GNR.

Defects affect not only carrier mobility but also other properties of 2D materials. As shown in Table 1.2, in the case of graphene, the characteristics such as Young's modulus, fracture strength, electrical conductivity, and thermal conductivity are sometimes greatly reduced when defects are present. Degradation by defects is similar phenomenon in other 2D materials. Therefore, people are trying to control defect to maintain the outstanding properties of 2D materials.

However, instead of this general approach, researches have tried to improve original properties or exhibit novel properties or phenomena that did not originally exist using the defects in materials. This approach is called *defect engineering*. Next, defect engineering in 2D materials will be described.

Table 1.2. Difference in performance between structurally perfect graphene and defective graphene. Reprinted with permission from [61]. Copyright 2018 Elsevier.

Properties	**Unit**	**Perfect graphene**	**Defective graphene**
Young's modulus	TPa	~ 1	0.15−0.95
Fracture strength	GPa	90−130	47−117
Electrical conductivity	S/m	10^8	$1-10^5$
Thermal conductivity	W/(m·K)	10^3-10^4	$10-10^3$

1.3. Defect engineering of 2D materials

Defects (in crystal) are imperfection in the regular geometrical arrangement of the atoms in a crystalline solid. The types of defects can be classified into point defects, line defects and plane defects according to their dimensionality. Many important properties of crystals can be derived from defects, including luminescence, diffusion, mechanical properties, and so on. When we remember that *engineering* is an application of knowledge, innovation, design, construction, operation and maintenance of structures, machines, materials, devices, systems, processes, and organization, the definition of *defect engineering* is as follows.

Defect + Engineering = ***Defect engineering***

*"Creating and manipulating **defects** to unlock the*

***full potential** of materials for applications"*

From here, we will look at some of the studies that take advantage of the effects. Y. Chen *et al.* reported bandgap modulation of TMD alloy [62]. They alloyed two TMD materials (MoS_2 and WS_2) with different bandgaps to make 2D alloy $Mo_{1-x}W_xS_2$ monolayer. They also carried out Photoluminescence (PL) measurements on the 2D alloy with various composition of Mo and W, then observed band gap emission continuously tuned from 1.82 eV to 1.99 eV (Figure 1.7). This is an example of adjusting the electronic properties through introducing defects.

Studies on optical properties of 2D materials using defects were also reported. C. Huang *et al.* reported improvements of optical properties of 2D TMD lateral heterostructures [63]. They synthesized high-quality lateral heterostructures using $MoSe_2$ and WSe_2 and carrier out PL measurements (Figure 1.8). Strong enhancement of PL signal was found at 1D heterointerface of lateral heterostructures (black arrow in Figure 1.8.a). They explained the reason why strong emission occurs is trapping

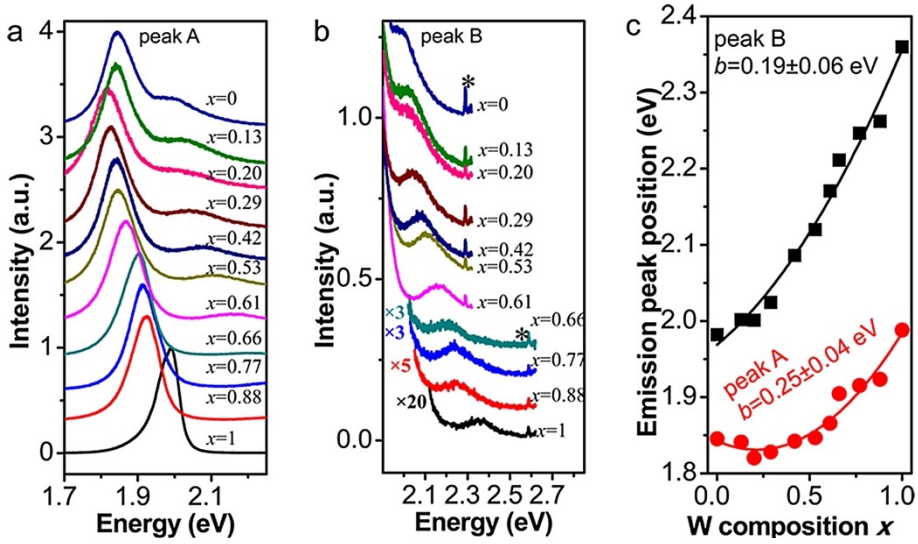

Figure 1.7. Composition-dependent PL emission from $Mo_{1-x}W_xS_2$ monolayers. a, b) PL spectra of $Mo_{1-x}W_xS_2$ monolayers with different W compositions x. The PL intensity is normalized by the maximum emission intensity (i.e., intensity of A exciton emission at 1.8−2.0 eV). The spectra were excited by 514.5 nm for x = 0−0.61 and 457.9 nm for x = 0.66−1. The peaks marked by * are Raman peaks of Si substrates. c) Composition-dependent emission energies for A and B excitons. The red and black lines are parabola fittings for composition-dependent energy of peaks A and B, giving a bowing parameter b of 0.25 ± 0.04 and 0.19 ± 0.06 eV, respectively. Reprinted with permission from [62]. Copyright 2013 American Chemical Society.

excitons by defects or enhanced radiative recombination at the interface.

Chemical properties can be enriched by the defects. Recently, people are trying to find a new hydrogen evolution reaction (HER) catalyst to replace platinum and among many candidates, MoS_2 is attracting a lot of attention. .J. Xie *et al.* suggested novel method to control defect in MoS_2 nanosheets using chemical treatments [64]. They synthesized defect-rich MoS_2 nanosheets (Figure 1.9.a) and confirmed that formation of defect-induced additional active edge sites. Thanks to additional active edge sites, HER efficiency of defect-rich MoS_2 nanosheets was remarkably increased than that of defect-free MoS_2 nanosheets (Figure 1.9.b).

Finally, magnetic properties were enriched by the defect. Z. Zhang *et al.* studied intrinsic magnetism of monolayer TMD induced by dislocation and grain boundaries (GBs) [65]. TMD materials do not show magnetic properties in general, but interestingly, dislocations and GBs could give new magnetic properties to it. Figure 1.10 shows that magnetic moments and stable magnetic ordering varies with respect to the tilt angle and type of GBs.

As discussed above, the use of defects can improve the inherent properties of 2D materials or discover new phenomena and properties.

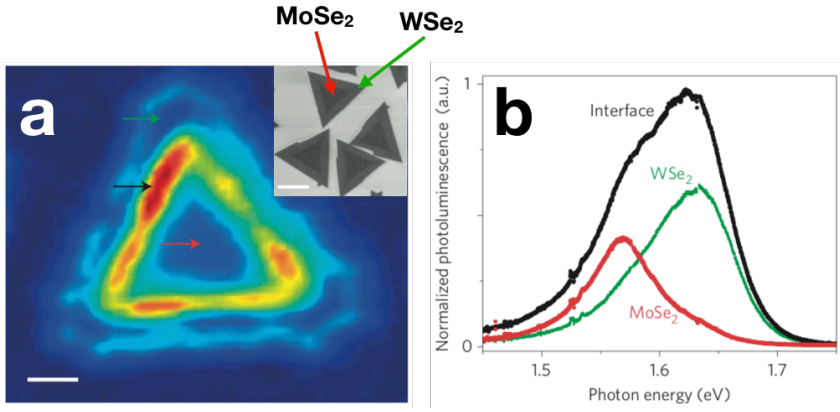

Figure 1.8. PL from 1D heterointerfaces. a) 2D PL intensity map of a triangular lateral heterostructure. Intense emission is seen from the 1D interface. Scanning micro-PL was performed with 532 nm laser excitation at room temperature. Inset: SEM images of heterostructure crystals from two different growths. All scale bars 10 μm. b) PL spectra taken at the points indicated by the corresponding colored arrows in a. Reprinted with permission from. Copyright 2014 Springer Nature.

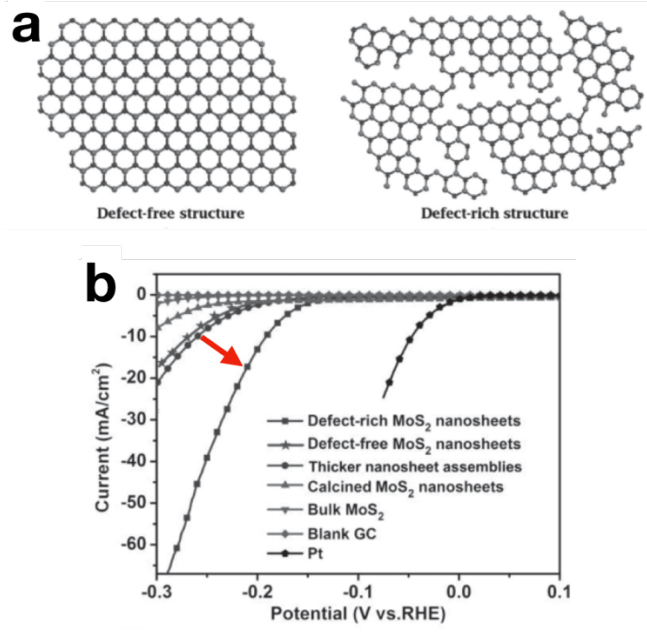

Figure 1.9. a) Structural models of defect-free and defect-rich structures. b) Polarization curves of various samples as indicated. Reprinted with permission from [64]. Copyright 2013 John Wiley & Sons.

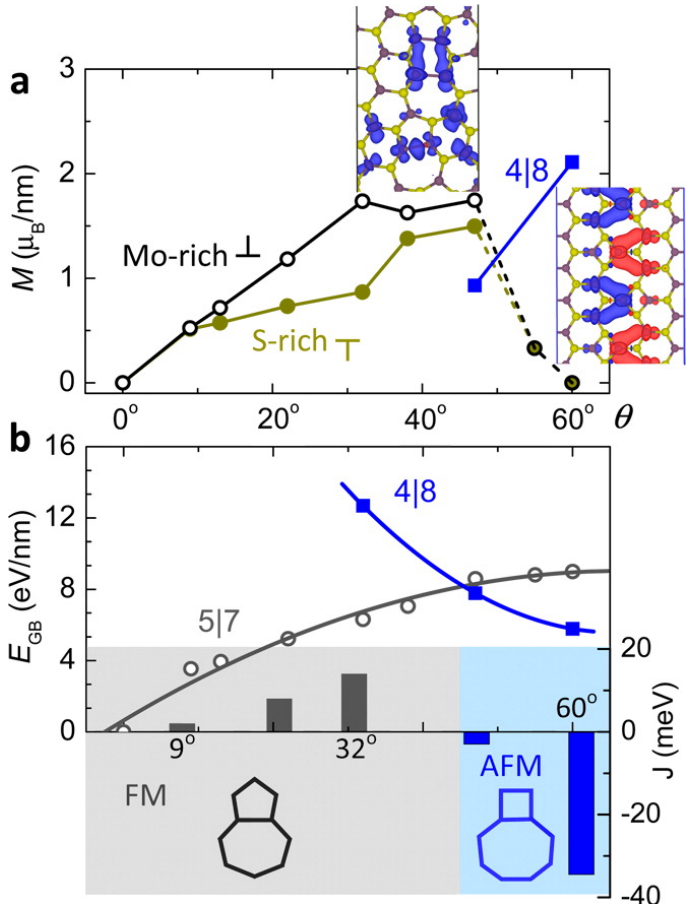

Figure 1.10. Tilt-dependent magnetism of GBs in MoS_2. a) Magnetic moment M per unit length of GB as a function of tilt angle. All values are obtained from GBs with FM order. Insets show magnetization densities (isovalue 2×10^{-3} e/Å^3) of a 38° GB composed of Mo-rich ⊥ and a 60° GB composed of 4|8s. b) Top left axis: energies of GBs as a function of θ, with gray circles for GBs composed of 5|7s and blue squares for GBs composed of 4|8s. Bottom right axis: exchange coupling parameter J for several typical GBs composed of Mo-rich ⊥ or 4|8s. Reprinted with permission from [65]. Copyright 2013 American Chemical Society.

1.4. Objective of the dissertation

In this dissertation, we present first-principles calculation studies on defect engineering of graphene and MoS_2. Defect induced structural and electronic properties of graphene and MoS_2 are mainly discussed in this dissertation.

First, we present deformation can control interaction between Fe dopants in monolayer graphene. The magnetic moment of Fe dopant pain covalently bonded to graphene lattice is changed dramatically by stretching or compressively bending graphene.

Second, we present stability and electronic properties of Cr and V substitutional dopants in monolayer MoS_2. We calculated formation energies of Cr and V substitutional dopants considering its charge states and possible chemical environments to investigate effects of Cr and V dopants on electronic properties of MoS_2.

Third, we introduce atomic-scale mechanism of structural phase transition of triangular MoS_2 nanocrystals. We investigated reaction mechanism of S vacancy formation by CO gas and established atomic-scale mechanism of structural phase transition from 2H to 1T in order to explain recent experimental results.

Thus, objective of this dissertation is investigating the effect of defect on structural and electronic properties of 2D materials and suggesting guidelines for novel applications of 2D materials.

1.5. Bibliography

[1] B. C. Brodie, Philos. Trans. R. Soc. London **149**, 249 (1859).

[2] G. Ruess and F. Vogt, Monatshefte Für Chemie **78**, 222 (1948).

[3] H. P. Boehm, A. Clauss, G. O. Fischer, and U. Hofmann, Zeitschrift Für Anorg. Und Allg. Chemie **316**, 119 (1962).

[4] K. S. Novoselov, Science (80-.). **306**, 666 (2004).

[5] K. S. Novoselov, A. K. Geim, S. V Morozov, D. Jiang, M. I. Katsnelson, I. V. Grigorieva, S. V. Dubonos, and A. A. Firsov, Nature **438**, 197 (2005).

[6] K. S. Novoselov, D. Jiang, F. Schedin, T. J. Booth, V. V. Khotkevich, S. V. Morozov, and A. K. Geim, Proc. Natl. Acad. Sci. **102**, 10451 (2005).

[7] D. Voiry, M. Salehi, R. Silva, T. Fujita, M. Chen, T. Asefa, V. B. Shenoy, G. Eda, and M. Chhowalla, Nano Lett. **13**, 6222 (2013).

[8] Y. Zhou and E. J. Reed, J. Phys. Chem. C **119**, 21674 (2015).

[9] A. Azizi, X. Zou, P. Ercius, Z. Zhang, A. L. Elías, N. Perea-López, G. Stone, M. Terrones, B. I. Yakobson, and N. Alem, Nat. Commun. **5**, 4867 (2014).

[10] M. Chhowalla, H. S. Shin, G. Eda, L.-J. Li, K. P. Loh, and H. Zhang, Nat. Chem. **5**, 263 (2013).

[11] Q. H. Wang, K. Kalantar-Zadeh, A. Kis, J. N. Coleman, and M. S. Strano, Nat. Nanotechnol. **7**, 699 (2012).

[12] J. Lin, S. T. Pantelides, and W. Zhou, ACS Nano **9**, 5189 (2015).

[13] B. Huang and H. Lee, Phys. Rev. B **86**, 245406 (2012).

[14] D. Pacilé, J. C. Meyer, Ç. Ö. Girit, and A. Zettl, Appl. Phys. Lett. **92**, 133107 (2008).

[15] K. H. Lee, H.-J. Shin, J. Lee, I. Lee, G.-H. Kim, J.-Y. Choi, and S.-W. Kim, Nano Lett. **12**, 714 (2012).

[16] A. Ismach, H. Chou, D. A. Ferrer, Y. Wu, S. McDonnell, H. C. Floresca, A. Covacevich, C. Pope, R. Piner, M. J. Kim, R. M. Wallace, L. Colombo, and R. S. Ruoff, ACS Nano **6**, 6378 (2012).

[17] O. Cretu, Y.-C. Lin, and K. Suenaga, Nano Lett. **14**, 1064 (2014).

[18] S. Okada, Phys. Rev. B **80**, 161404 (2009).

[19] Y. Stehle, H. M. Meyer, R. R. Unocic, M. Kidder, G. Polizos, P. G. Datskos, R. Jackson, S. N. Smirnov, and I. V Vlassiouk, Chem. Mater. **27**, 8041 (2015).

[20] H. Liu, Y. Du, Y. Deng, and P. D. Ye, Chem. Soc. Rev. **44**, 2732 (2015).

[21] Y. Li and X. Chen, 2D Mater. **1**, 31002 (2014).

[22] J. Guan, Z. Zhu, and D. Tománek, ACS Nano **8**, 12763 (2014).

[23] V. Sorkin and Y. W. Zhang, Nanotechnology **26**, 235707 (2015).

[24] H. Liu, A. T. Neal, Z. Zhu, Z. Luo, X. Xu, D. Tománek, and P. D. Ye, ACS Nano **8**, 4033 (2014).

[25] A. Manjanath, A. Samanta, T. Pandey, and A. K. Singh, Nanotechnology **26**, 1 (2015).

[26] K. F. Mak, C. Lee, J. Hone, J. Shan, and T. F. Heinz, Phys. Rev. Lett. **105**, 136805 (2010).

[27] A. Splendiani, L. Sun, Y. Zhang, T. Li, J. Kim, C.-Y. Chim, G. Galli, and F. Wang, Nano Lett. **10**, 1271 (2010).

[28] M. A. Lukowski, A. S. Daniel, F. Meng, A. Forticaux, L. Li, and S. Jin, J. Am. Chem. Soc. **135**, 10274 (2013).

[29] J. Zhang, J. Wu, H. Guo, W. Chen, J. Yuan, U. Martinez, G. Gupta, A. Mohite, P. M. Ajayan, and J. Lou, Adv. Mater. **29**, 1701955 (2017).

[30] Q. Tang and D. Jiang, ACS Catal. **6**, 4953 (2016).

[31] B. Huang, H. Xiang, J. Yu, and S.-H. Wei, Phys. Rev. Lett. **108**, 206802 (2012).

[32] L. Banszerus, M. Schmitz, S. Engels, J. Dauber, M. Oellers, F. Haupt, K. Watanabe, T. Taniguchi, B. Beschoten, and C. Stampfer, Sci. Adv. **1**, e1500222 (2015).

[33] H. Y. Hwang, Y. Iwasa, M. Kawasaki, B. Keimer, N. Nagaosa, and Y. Tokura, Nat. Mater. **11**, 103 (2012).

[34] M. Osada and T. Sasaki, J. Mater. Chem. **19**, 2503 (2009).

[35] W. Feng, X. Wang, J. Zhang, L. Wang, W. Zheng, P. Hu, W. Cao, and B. Yang, J. Mater. Chem. C **2**, 3254 (2014).

[36] A. J. Mannix, X. F. Zhou, B. Kiraly, J. D. Wood, D. Alducin, B. D. Myers, X. Liu, B. L. Fisher, U. Santiago, J. R. Guest, M. J. Yacaman, A. Ponce, A. R. Oganov, M. C. Hersam, and N. P. Guisinger, Science (80-.). **350**, 1513

(2015).

[37] S. Xu, Y. Zhao, J. Liao, X. Yang, and H. Xu, Nano Res. **9**, 2616 (2016).

[38] Z. Ni, Q. Liu, K. Tang, J. Zheng, J. Zhou, R. Qin, Z. Gao, D. Yu, and J. Lu, Nano Lett. **12**, 113 (2012).

[39] M. Houssa, G. Pourtois, V. V. Afanas'ev, and A. Stesmans, Appl. Phys. Lett. **96**, 082111 (2010).

[40] L. Li, S. Lu, J. Pan, Z. Qin, Y. Wang, Y. Wang, G. Cao, S. Du, and H.-J. Gao, Adv. Mater. **26**, 4820 (2014).

[41] S. Bae, H. Kim, Y. Lee, X. Xu, J.-S. Park, Y. Zheng, J. Balakrishnan, T. Lei, H. Ri Kim, Y. Il Song, Y.-J. Kim, K. S. Kim, B. Özyilmaz, J.-H. Ahn, B. H. Hong, and S. Iijima, Nat. Nanotechnol. **5**, 574 (2010).

[42] K. S. Kim, Y. Zhao, H. Jang, S. Y. Lee, J. M. Kim, K. S. Kim, J.-H. Ahn, P. Kim, J.-Y. Choi, and B. H. Hong, Nature **457**, 706 (2009).

[43] L. Li, Y. Yu, G. J. Ye, Q. Ge, X. Ou, H. Wu, and … D. F., Nat. Nanotechnol. (2014).

[44] E. V Castro, K. S. Novoselov, S. V Morozov, N. M. R. Peres, J. M. B. L. dos Santos, J. Nilsson, F. Guinea, A. K. Geim, and A. H. C. Neto, Phys. Rev. Lett. **99**, 216802 (2007).

[45] F. Bonaccorso, Z. Sun, T. Hasan, and A. C. Ferrari, Nat. Photonics **4**, 611 (2010).

[46] F. Xia, H. Wang, and Y. Jia, Nat. Commun. **5**, (2014).

[47] H. Wang, Y. Yang, Y. Liang, J. T. Robinson, Y. Li, A. Jackson, Y. Cui, and H. Dai, Nano Lett. **11**, 2644 (2011).

[48] H. J. Yan, B. Xu, S. Q. Shi, and C. Y. Ouyang, J. Appl. Phys. **112**, 104316 (2012).

[49] S. Homaeigohar and M. Elbahri, NPG Asia Mater. **9**, e427 (2017).

[50] L. Cao, L. Cheng, Z. Zhang, Y. Wang, X. Zhang, H. Chen, B. Liu, S. Zhang, and J. Kong, Lab Chip **12**, 4864 (2012).

[51] Y. Ohno, K. Maehashi, and K. Matsumoto, J. Am. Chem. Soc. **132**, 18012 (2010).

[52] O. Lopez-Sanchez, D. Lembke, M. Kayci, A. Radenovic, and A. Kis, Nat. Nanotechnol. **8**, 497 (2013).

[53] L. Ji, Z. Tan, T. Kuykendall, E. J. An, Y. Fu, V. Battaglia, and Y. Zhang,

Energy Environ. Sci. **4**, 3611 (2011).

[54] D. Kim, S. Park, I. Jo, S.-M. Kim, D. H. Kang, S.-P. Cho, J. B. Park, B. H. Hong, and M.-H. Yoon, Small **13**, 1700331 (2017).

[55] J.-H. Chen, C. Jang, S. Xiao, M. Ishigami, and M. S. Fuhrer, Nat. Nanotechnol. **3**, 206 (2008).

[56] J. Hwang, C. Kuo, L.-C. Chen, and K.-H. Chen, Nanotechnology **21**, 465705 (2010).

[57] A. Betti, G. Fiori, and G. Iannaccone, IEEE Trans. Electron Devices **58**, 2824 (2011).

[58] F. Chen, J. Xia, D. K. Ferry, and N. Tao, Nano Lett. **9**, 2571 (2009).

[59] A. S. Mayorov, R. V. Gorbachev, S. V. Morozov, L. Britnell, R. Jalil, L. A. Ponomarenko, P. Blake, K. S. Novoselov, K. Watanabe, T. Taniguchi, and A. K. Geim, Nano Lett. **11**, 2396 (2011).

[60] C.-C. Lu, Y.-C. Lin, C.-H. Yeh, J.-C. Huang, and P.-W. Chiu, ACS Nano **6**, 4469 (2012).

[61] T. Xu and L. Sun, in *Defects Adv. Electron. Mater. Nov. Low Dimens. Struct.* (Elsevier, 2018), pp. 137–160.

[62] Y. Chen, J. Xi, D. O. Dumcenco, Z. Liu, K. Suenaga, D. Wang, Z. Shuai, Y.-S. Huang, and L. Xie, ACS Nano **7**, 4610 (2013).

[63] C. Huang, S. Wu, A. M. Sanchez, J. J. P. Peters, R. Beanland, J. S. Ross, P. Rivera, W. Yao, D. H. Cobden, and X. Xu, Nat. Mater. **13**, 1096 (2014).

[64] J. Xie, H. Zhang, S. Li, R. Wang, X. Sun, M. Zhou, J. Zhou, X. W. D. Lou, and Y. Xie, Adv. Mater. **25**, 5807 (2013).

[65] Z. Zhang, X. Zou, V. H. Crespi, and B. I. Yakobson, ACS Nano **7**, 10475 (2013).

Chapter 2. Theoretical background

2.1. Density functional theory

The physical properties of the materials are governed by many-body Schrödinger equation. However, many-body Schrödinger equation cannot be solved only by analytical method but also numerical approaches because of its complexity. Density functional theory is the one of the main approaches to solve many-body Schrödinger equation numerically and has recently been used as an indispensable tool in physics, chemistry, materials science, and various fields. In the following, main idea and scheme of the DFT will be introduced.

2.1.1. Hohenberg-Kohn theorem

Many-body Schrödinger equation can be written as

$$\left[-\frac{1}{2}\sum_i \nabla_i^2 + \sum_i V_{\text{ext}}(\mathbf{r}_i) + \frac{1}{2}\sum_{i\neq j}\frac{1}{|\mathbf{r}_i-\mathbf{r}_j|}\right]\Psi_n(\{\mathbf{r}_i\}) = E_n\Psi_n(\{\mathbf{r}_i\}) \quad (2.1)$$

where an external potential $V_{\text{ext}}(\mathbf{r}_i)$ includes any problem of electrons and fixed nuclei. Hohenberg-Kohn suggested two theorems, which is basis for the DFT, as following [1,2].

Theorem I: For any system of interacting particles in an external potential $V_{\text{ext}}(\mathbf{r})$ is determined uniquely, except for a constant, by the ground state particle density $n_0(\mathbf{r})$.

Corollary I: Since the Hamiltonian is thus fully determined, except for a constant shift of the energy, it follows that the many-body wavefunctions for all states (ground and excited) are determined. *Therefore, all properties of the system are completely determined given only the ground state density* $n_0(\mathbf{r})$.

Theorem II: A *universal functional* for the energy $E[n]$ in terms of the density $n(\mathbf{r})$ can be defined, valid for any external potential $V_{\text{ext}}(\mathbf{r})$. For any particular $V_{\text{ext}}(\mathbf{r})$, the exact ground state energy of the system is the global minimum value of this functional, and the density $n(\mathbf{r})$ that minimizes the functional is the exact ground state density $n_0(\mathbf{r})$.

Corollary II: The functional $E[n]$ alone is sufficient to determine the exact ground state energy and density. In general, excited states of the electrons must be determined by other means.

All properties of the system are uniquely determined if $n(\mathbf{r})$ is specified, thus each property can be regarded as a functional of $n(\mathbf{r})$. One example is the total energy functional can be written as

$$\begin{aligned} E_{\text{HK}}[n] &= T[n] + E_{\text{int}}[n] + \int d^3r\, V_{\text{ext}}(\mathbf{r})n(\mathbf{r}) + E_{\text{Ion-Ion}} \\ &\equiv F_{\text{HK}}[n] + \int d^3r\, V_{\text{ext}}(\mathbf{r})n(\mathbf{r}) + E_{\text{Ion-Ion}} \end{aligned} \tag{2.2}$$

where $E_{\text{Ion-Ion}}$ is the interaction energy of the nuclei. The functional $F_{\text{HK}}[n]$ defined in (2.2) includes all internal energies, kinetic and potential, of the interacting electron system,

$$F_{\text{HK}}[n] = T[n] + E_{\text{int}}[n] \tag{2.3}$$

which must be universal by construction since the kinetic energy and interaction energy of the particles are functionals only of the density. If the functional $F_{\text{HK}}[n]$ was known, the by minimizing the total energy of the system, (2.2), with respect to variations in the densify function $n(\mathbf{r})$, one would find the exact ground state density and energy.

2.1.2. Kohn-Sham equation

In 1965, Kohn and Sham suggested replacing the difficult interacting many-body system with a different *auxiliary system* that can be solved more easily [3]. Kohn and Sham chose independent-particle equations for the non-interacting system that can be considered exactly soluble with all the difficult many-body terms incorporated into an *exchange-correlation functional* of the density.

The Kohn-Sham approach to the full interacting many-body problem is to rewire the Hohenberg-Kohn expression for the ground state energy functional (2.2) in the form

$$E_{\mathrm{KS}} = T_s[n] + \int d\mathbf{r} V_{ext}(\mathbf{r}) n(\mathbf{r}) + \frac{1}{2}\int d^3r d^3r' \frac{n(\mathbf{r})n(\mathbf{r}')}{|\mathbf{r}-\mathbf{r}'|} + E_{\text{Ion-Ion}} + E_{xc}[n] \quad (2.4)$$

where $T_s[n]$ is the independent-particle kinetic energy and $V_{ext}(\mathbf{r})$ is the external potential due to the nuclei and any other external fields and $E_{\text{Ion-Ion}}$ is the interaction between the nuclei, and third term is the $E_{\text{Hartree}}[n]$.

Minimizing (2.4) leads to the Schrödinger-like Kohn-Sham equations:

$$(H_{\mathrm{KS}} - \epsilon_i)\psi_i(\mathbf{r}) = 0 \quad (2.5)$$

where the ϵ_i are the eigenvalues, and H_{KS} is the effective Hamiltonian

$$H_{\mathrm{KS}}(\mathbf{r}) = -\frac{1}{2}\nabla^2 + V_{\mathrm{KS}}(\mathbf{r}) \quad (2.6)$$

with

$$\begin{aligned} V_{\mathrm{KS}}(\mathbf{r}) &= V_{\mathrm{ext}}(\mathbf{r}) + \frac{\delta E_{\mathrm{Hartree}}}{\delta n(\mathbf{r})} + \frac{\delta E_{\mathrm{xc}}}{\delta n(\mathbf{r})} \\ &= V_{\mathrm{ext}}(\mathbf{r}) + V_{\mathrm{Hartree}}(\mathbf{r}) + V_{\mathrm{xc}}(\mathbf{r}). \end{aligned} \quad (2.7)$$

Equations (2.5) − (2.7) are the well-known Kohn-Sham equations, with the resulting total energy E_{KS} given by (2.4) and density $n(\mathbf{r})$ as

$$n(\mathbf{r}) = \sum_{i=1}^{N} |\psi_i(\mathbf{r})|^2. \qquad (2.8)$$

2.1.3. Exchange-correlation energy

The crucial quantity in the Kohn-Sham approach is the exchange-correlation energy which is expressed as a functional of the density $E_{\mathrm{xc}}[n]$. Two conventional approximations for the exchange-correlation energy are widely used, which are local density approximation (LDA) and generalized gradient approximation (GGA).

LDA was first suggested by Kohn and Sham [3], in which the exchange-correlation energy is simply an integral over all space with the exchange-correlation energy density at each points assumed to be the same as in a homogeneous electron gas with that density,

$$E_{\mathrm{xc}}^{\mathrm{LDA}}[n] = \int d^3r n(\mathbf{r})\epsilon_{\mathrm{xc}}\big(n(\mathbf{r})\big). \qquad (2.9)$$

LDA is best for solids close to a homogeneous gas (like a nearly-free-electron metal) and worst for very inhomogeneous cases like atoms where the density must go continuously to zero outside the atom. One more noticeable fault is the spurious self-interaction term. In the LDA, the unphysical self-term in the Hartree interaction is cancelled only approximate and there remain spurious self-interaction terms that are negligible in the homogeneous gas but large in confined systems such as atoms. Usually, the bond strength or the lattice parameter is underestimated than experiments.

The success of the LDA has led to the development of various GGA with marked improvement over LDA for many cases. The term generalized gradient expansion denotes a variety of ways proposed for functions that modify the behavior at large gradients in such a way as to preserve desired properties. It is convenient to define the functional as a generalized form of (2.9) [4].

$$E_{\mathrm{xc}}^{\mathrm{GGA}}[n] = \int d^3r n(\mathbf{r})\epsilon_{\mathrm{xc}}(n(\mathbf{r}), |\nabla n(\mathbf{r})|, \dots) \qquad (2.10)$$

Numerous kinds of GGA have been proposed; these can be illustrated by the tree widely used forms of Becke (B88) [5], Perdew and Wang (PW91) [6], and Perdew, Burke, and Ernzerhof (PBE) [7]. Typically, there are more rapidly varying density regions in atoms than in condensed matter, which leads to greater lowering of the exchange energy in atoms than in molecules and solids. This results in the reduction of binding energy, correcting the LDA overbinding, and improving agreement with experiment, which is one of the most important characteristics of present GGAs [8].

2.2. Supercell calculations for neutral and charged defects

Periodic boundary conditions allow fast density functional based calculations for defects and their complexes in materials. Defect energetics, structural parameters, vibrational modes and other physical characteristics can be estimated by these calculations. However, if defects are present in the small unit cell, the periodicity cause spurious defect-defect interactions and dispersion of the defect-induced electronic states [9].

To overcome these problems, extended crystal unit cell of appropriate size should be used. If we use small crystal unit cell (primitive or conventional), distance between neighboring defects in periodic image is small so that spurious interactions between neighboring defects (vacancy sites in Figure 2.1.) become significant. However, if we extend unit cell to supercell of appropriate size, distance between neighboring defects in periodic images gets far away enough to give correct results. Therefore, supercell method is indispensable tool for defects calculations.

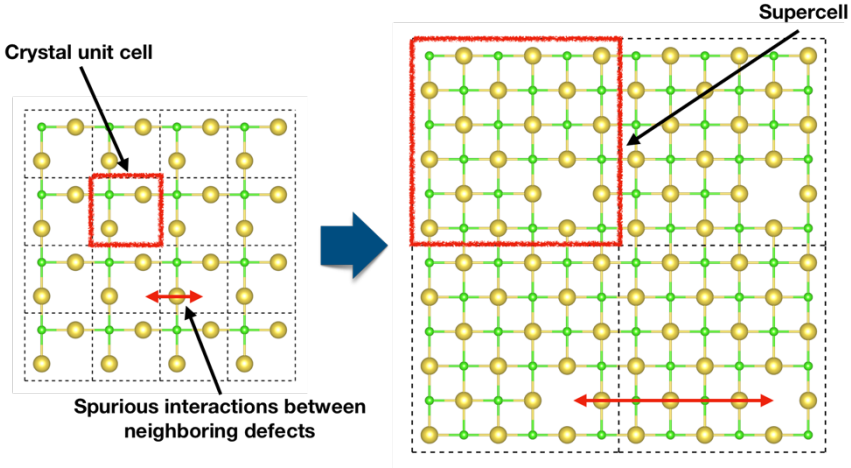

Figure 2.1. Schematic interpretation of the supercell calculations for defects

For charged defects, the situation is more complicated. Long-range Coulomb interactions between periodic image charges continue to exist in sufficient large supercell so appropriate correction should be taken into account to obtain desired properties of the isolated defects (i.e. a single defect in infinite unit cell). Several studies have been carried out and succeeded, especially for the bulk system [10–14].

Formula for the formation energy of isolated defects in charge state q [15] can be written as

$$E_{\text{form}} = E_{\text{total}}^{\text{defect}} - E_{\text{total}}^{\text{perfect}} + \sum_i n_i \mu_i + q\left(E_{\text{VBM}}^{\text{perfect}} + E_{\text{Fermi}}\right) + E_{\text{corr}} \quad (2.11)$$

where $E_{\text{total}}^{\text{defect}}$ is the total energy of the supercell containing the defect, and $E_{\text{total}}^{\text{perfect}}$ is the total energy for the perfect crystal of same supercell. The integer n_i means the number of atoms of type *i* that have been added ($n_i > 0$) or removed ($n_i < 0$) from the supercell to create the defect, and the μ_i are the chemical potentials of type *i*. Chemical potentials characterize the energy of the reservoirs for the exchanging species. $E_{\text{VBM}}^{\text{perfect}}$ is the valence band maximum of the perfect host material and E_{Fermi} is the Fermi level with the reference to the $E_{\text{VBM}}^{\text{perfect}}$, that means $E_{\text{VBM}}^{\text{perfect}} + E_{\text{Fermi}}$ indicates the chemical potential for the electrons. E_{corr} is the correction term containing electrostatic interactions between image charges and the potential level alignment between model charge system and DFT calculations.

In chapter 4 of this dissertation, finite-size supercell correction for charged defects at surfaces and interfaces was used [16,17]. Unlike defects in the bulk system, if defects present in surface or interface of host material, inhomogeneous dielectric environments have to be considered. Dielectric constant profile can be obtained from the densify functional perturbation theory (DFPT) calculations [18,19].

E_{corr} can be written as

$$E_{\text{corr}} = E_{\text{model}}^{\text{isolated}} - E_{\text{model}}^{\text{supercell}} + q\Delta V \quad (2.12)$$

where contains electrostatic energy difference between the isolated (open boundary) and supercell-sized model charge system $E_{\text{model}}^{\text{isolated}} - E_{\text{model}}^{\text{supercell}}$ and potential difference ΔV between the electrostatic potential $V_{\text{model}}(\mathbf{r})$ in the model charge system and DFT calculated Hartree potential $V_{\text{DFT}}(\mathbf{r})$ that is induced only by the charged defect, far from the defect site.

Form of model charge is not critical [12,14] so Gaussian charge distribution was used. Electrostatic potential of the model charge system $V_{\text{model}}(\mathbf{r})$ can be obtained by solving Poisson equation written as

$$\nabla \cdot [\epsilon(\mathbf{r})\nabla V_{\text{model}}(\mathbf{r})] = -4\pi\rho(\mathbf{r}) \quad (2.13)$$

where $\rho(\mathbf{r})$ is the charge density and $\epsilon(\mathbf{r})$ is the dielectric constant profile calculated from DFPT. Electrostatic energy of supercell-sized model charge system can be calculated as

$$E_{\text{model}}^{\text{supercell}} = \frac{1}{2}\int d^3\mathbf{r}\rho(\mathbf{r})V_{\text{model}}(\mathbf{r}). \quad (2.14)$$

$E_{\text{model}}^{\text{supercell}}$ was calculated for supercell of various size (supercell size ~ $1/\alpha$) and fitted to fifth-order polynomial written as

$$E_{\text{model}} = E_{\text{model}}^{\text{isolated}} + \frac{s_1}{\alpha} + \frac{s_2}{\alpha^2} + \frac{s_3}{\alpha^3} + \frac{s_4}{\alpha^4} + \frac{s_5}{\alpha^5} \quad (2.15)$$

where s_i are fitting parameters to obtain electrostatic energy of isolated charge

in an infinite-sized supercell $E_{\mathrm{model}}^{\mathrm{isolated}}$.

The potential difference ΔV in (2.12) is considered at far from the defect site. It can be written as

$$\Delta V = [V_{\mathrm{model}}(\mathbf{r}) - V_{\mathrm{DFT}}(\mathbf{r})]_{\mathbf{r}=\mathrm{far}} \qquad (2.16)$$

where $V_{\mathrm{DFT}}(\mathbf{r})$ can be decomposed as

$$\begin{aligned} V_{\mathrm{DFT}}(\mathbf{r}) &= V_{\mathrm{DFT}}^{q}(\mathbf{r}) + V_{\mathrm{DFT}}^{0}(\mathbf{r}) \\ &= [V_{\mathrm{Hartree}}^{\mathrm{defect}(q\neq 0)}(\mathbf{r}) - V_{\mathrm{Hartree}}^{\mathrm{defect}(q=0)}(\mathbf{r})] \\ &\quad + [V_{\mathrm{Hartree}}^{\mathrm{defect}(q=0)}(\mathbf{r}) - V_{\mathrm{Hartree}}^{\mathrm{perfect}}(\mathbf{r})]. \end{aligned} \qquad (2.17)$$

The $V_{\mathrm{DFT}}^{q}(\mathbf{r})$ is the DFT Hartree potential induced only by the excess charge of the defect, and $V_{\mathrm{DFT}}^{0}(\mathbf{r})$ only by the neutral defect itself.

2.3. Bibliography

[1] P. Hohenberg and W. Kohn, Phys. Rev. **136**, B864 (1964).

[2] R. M. Martin, *Electronic Structure* (Cambridge University Press, Cambridge, 2004).

[3] W. Kohn and L. J. Sham, Phys. Rev. **140**, A1133 (1965).

[4] J. P. Perdew and K. Burke, Int. J. Quantum Chem. **57**, 309 (1996).

[5] A. D. Becke, Phys. Rev. A **38**, 3098 (1988).

[6] J. P. Perdew and Y. Wang, Phys. Rev. B **45**, 13244 (1992).

[7] J. P. Perdew, K. Burke, and M. Ernzerhof, Phys. Rev. Lett. **77**, 3865 (1996).

[8] W. Koch and M. C. Holthausen, *A Chemist's Guide to Density Functional Theory* (Wiley-VCH Verlag GmbH, Weinheim, FRG, 2001).

[9] R. M. Nieminen, in *Theory Defects Semicond.* (Springer Berlin Heidelberg, 2006), pp. 29–68.

[10] G. Makov and M. C. Payne, Phys. Rev. B **51**, 4014 (1995).

[11] S. Lany and A. Zunger, Phys. Rev. B **78**, 235104 (2008).

[12] C. Freysoldt, J. Neugebauer, and C. G. Van de Walle, Phys. Rev. Lett. **102**, 016402 (2009).

[13] S. E. Taylor and F. Bruneval, Phys. Rev. B **84**, 075155 (2011).

[14] H.-P. Komsa, T. T. Rantala, and A. Pasquarello, Phys. Rev. B **86**, 045112 (2012).

[15] C. Freysoldt, B. Grabowski, T. Hickel, J. Neugebauer, G. Kresse, A. Janotti, and C. G. de Walle, Rev. Mod. Phys. **86**, 253 (2014).

[16] H.-P. Komsa and A. Pasquarello, Phys. Rev. Lett. **110**, 095505 (2013).

[17] J.-Y. Noh, H. Kim, and Y.-S. Kim, Phys. Rev. B **89**, 205417 (2014).

[18] S. Baroni and R. Resta, Phys. Rev. B **33**, 7017 (1986).

[19] M. Gajdoš, K. Hummer, G. Kresse, J. Furthmüller, and F. Bechstedt, Phys. Rev. B **73**, 045112 (2006).

Chapter 3. Deformation induced control of interaction between Fe dopants in monolayer graphene

3.1. Motivation

Graphene has gained significant interest due to its unique electronic, mechanical, chemical, and magnetic properties related to its 2D structure [1,2]. Since the fabrication of graphene [3], a variety of industrial applications have been proposed [4–10]. Graphene's robust flexibility makes it suitable for a wide range of flexible device applications [11–13]. As one of best materials for future flexible electronics, graphene has possibilities for integration into wearable electronic devices [11,13], flexible displays [6], and batteries [7,8]. Stretching and bending of 2D films such as graphene induces a strain that can modify the bonding and interaction between atoms and molecules that are adsorbed on the surface. Adatoms and molecules are often found residing on the surface of graphene, but they are only bound by weak van der Waals forces and can easily be removed at high temperature or under vacuum conditions.

However, substitutional dopants in graphene are strongly covalently bonded to the carbon atoms and thus provide a robust system. Recent reports showed that paramagnetic metal atoms can be trapped by vacancy in graphene and form stable covalent dopants [14]. The graphene vacancy is also considered to be an effective bonding site for other elements, such as Fe [15–17], Si [18,19], and N [20,21], which form covalent bonds to the under-coordinated carbon atoms. These atomic dopants have been directly imaged and verified using aberration corrected transmission electron microscopy (AC-TEM) and electron energy loss spectroscopy. Since graphene is flexible it should be possible to control the interaction between doped atoms in graphene by introducing a strain through flexing of the graphene sheet.

Recently, ferromagnetic metal atoms doped in graphene were observed using AC-TEM [15,16], and it was reported by density functional theory (DFT) calculations that the various magnetic moments depended on the structural configurations of the dopants [16]. Pairs of Fe atom dopants in graphene showed more consistent magnetic moments compared to the isolated single Fe dopants, with only small variations that depended on the type of carbon atoms missing around the Fe pair [16]. While a single isolated Fe atom substituted in monovacancy (Fe@MV, Figure 3.1.a) has no magnetic moment [16,22], two neighboring Fe atoms substituted into two monovacancy sites (DiFe@2MV, Figure 3.1.b) give a magnetic moment of 2 μ_B. Increasing the separation between the two Fe dopant sites causes the magnetic moment to drop dramatically, and suggests that fine control over the spatial separation should lead to significant changes in the magnetic moment generated by this pair.

In this chapter, we use DFT calculation methods to explore the possibility of controlling the fine scale distance between two Fe substitutional dopants in order to manipulate the total magnetic moment by stretching or compressing the graphene lattice through flexural bending of the sheet. Most of papers about magnetic properties in graphene are focused on the adatom on perfect graphene [23,24]. However, in this chapter, we study the magnetic properties of metal dopants in graphene vacancy sites and the changes of magnetic properties depending on the stretching and compressing of graphene.

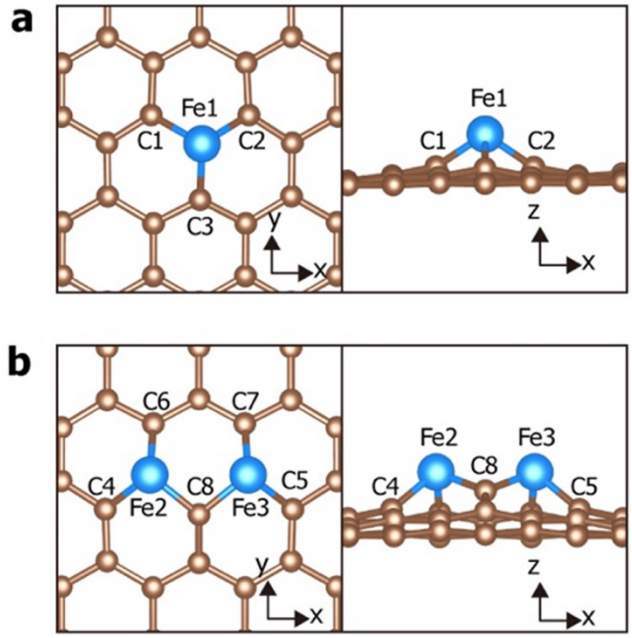

Figure 3.1. Structural models of Fe dopants in graphene. (a) One Fe atom dopant in a monovacancy (Fe@MV). (b) Two Fe atoms dopants in two neighboring monovacancies (DiFe@2MV). Letters with numbers are given to atoms for the explanation of partial density of states (PDOS) in Figure 3.4. Reprinted with permission from [25]. Copyright 2017 IOP Publishing.

3.2. Computational details

We performed spin-polarized calculations within the generalized gradient approximation (GGA) of the Perdew−Burke−Ernzerhof (PBE) functional [26] using Vienna ab initio simulation package (VASP) code [27]. The unit cell containing two Fe atoms in two monovacancies was constructed from pristine graphene of 200 carbon atoms. In constructing the supercell for simulation, we included a vacuum region of 30 Å in the *z* direction. The basis set contained plane waves up to an energy cutoff of 400 eV. The Brillouin zone was sampled using a 3×3×1 Γ-centered mesh. For geometrical optimization, all atomic positions were fully relaxed until the force on each atom was smaller than 0.02 eV/Å while the extended or contracted unit cell size was fixed in the case of stretching or compressing graphene. For the stretching of graphene, we proportionally extended the unit cell along the *x*-axis (zigzag direction) in which two Fe atoms lay along the *x*-axis. To express the bending of graphene in our simulation, we constructed two types of the unit cell, inwards bending and outward bending to make concave and convex structures, respectively. We also proportionally contracted the unit cell along the *x*-axis to simulate the bending of graphene.

3.3. Results and discussion

3.3.1. Magnetic properties control of Fe dopants through structural deformations of graphene

We performed DFT calculations for a Fe@MV and found the total magnetic moment to be zero, consistent with previous reports [16,22]. In the optimized geometry, a Fe atom is located at the center of the vacancy in the *xy* plane and protrudes at a height of 1.2 Å from the graphene plane (Figure 3.1.a). The DFT calculation for DiFe@2MV found the total magnetic moment to be 2 μ_B, it is also consistent with previous report [16]. In the structure of DiFe@2MV, both Fe atoms located at the center of each vacancy and also protruding at height 2.1 Å from the graphene plane (Figure 3.1.b). To elucidate origin of magnetic moments of DiFe@2MV and consider stretching and compressing effects to magnetic properties, we first confirmed previous results of Fe@MV and DiFe@2MV.

The presence of a magnetic moment in DiFe@2MV is likely due to the interaction between the two Fe dopant atoms. To study the interaction between the Fe atoms in a DiFe@2MV, we separate the two constituent Fe@MVs of the defect to and calculate the magnetic moment to be 0 μ_B, the same as the magnetic moment of a single isolated Fe@MV.

We also calculate the magnetic moment when decreasing the distance between two Fe@MVs and find that the magnetic moment is still zero up until the two Fe@MVs come to the distance of only one zigzag spacing more than the distance between two Fe atoms in a DiFe@2MV. This indicates that there is a critical distance for Fe-Fe interactions related to the existence of a magnetic moment in a DiFe@2MV.

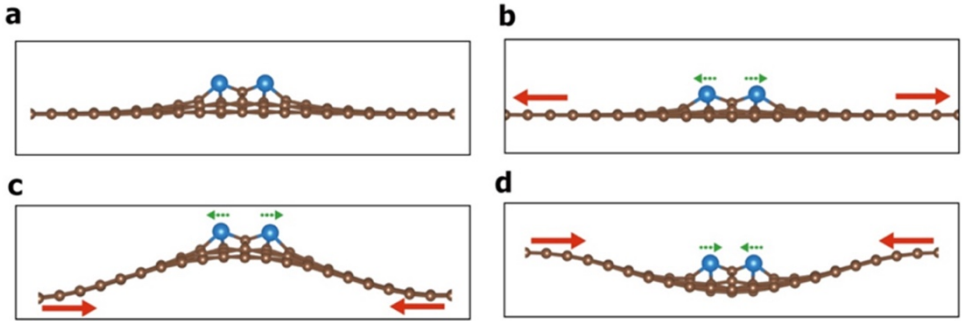

Figure 3.2. Schematic diagrams for change of Fe-Fe distance by stretching and compressing graphene. (a) Pristine graphene, (b) stretched graphene, (c) graphene under compressive outward bending, and (d) graphene under compressive inwards bending. Red arrows indicate stretching or compressing. Green dotted arrows indicate the increase or decrease of Fe-Fe distance depending on stretching or compressing, respectively. Reprinted with permission from [25]. Copyright 2017 IOP Publishing.

By stretching and bending the host graphene lattice we can modify the separation of the Fe atoms through strain of the lattice, shown in Figure 3.2. In the case of compression bending of graphene is induced, with two possible bending directions, shown in Figures 3.2.c and d. Stretching graphene in-plane (i.e. *x* direction) modified the Fe-Fe distance within the DiFe@2MV and the subsequent change to the magnetic moment is calculated by DFT calculation methods.

In the calculation the size of the unit cell is varied to represent stretching of the graphene, and we then relax atomic positions and calculate the magnetic moment. As shown in figure 3.3.a, we found the magnetic moment starts to decrease at a stretching ratio of 2.72% and disappears for a stretching ratio of 4.23%, which corresponds to a critical Fe-Fe distance of 2.79 Å. While the Fe-Fe distance increases monotonically as the stretching ratio increases, it increases quickly and irregularly near the critical distance value, which is considered to be due to the magnetic instability near the critical distance.

As another trial for the control of Fe-Fe distance, we also compress the graphene membrane to induce an outward bending mode as shown in Figure 3.2.c, which essentially causes an increase in the Fe-Fe distance. The changes of the magnetic moment and Fe-Fe distance are shown in Figure 3.3.b. In this case, the magnetic moment disappears at a compressing ratio of 1.50% which corresponds to a Fe-Fe critical distance of 2.82 Å. The magnetic moment changes faster when the graphene membrane is bent (Figures 3.2.c and 3.3.b) compared to just stretching in plane (Figures 3.2.b and 3.3.a).

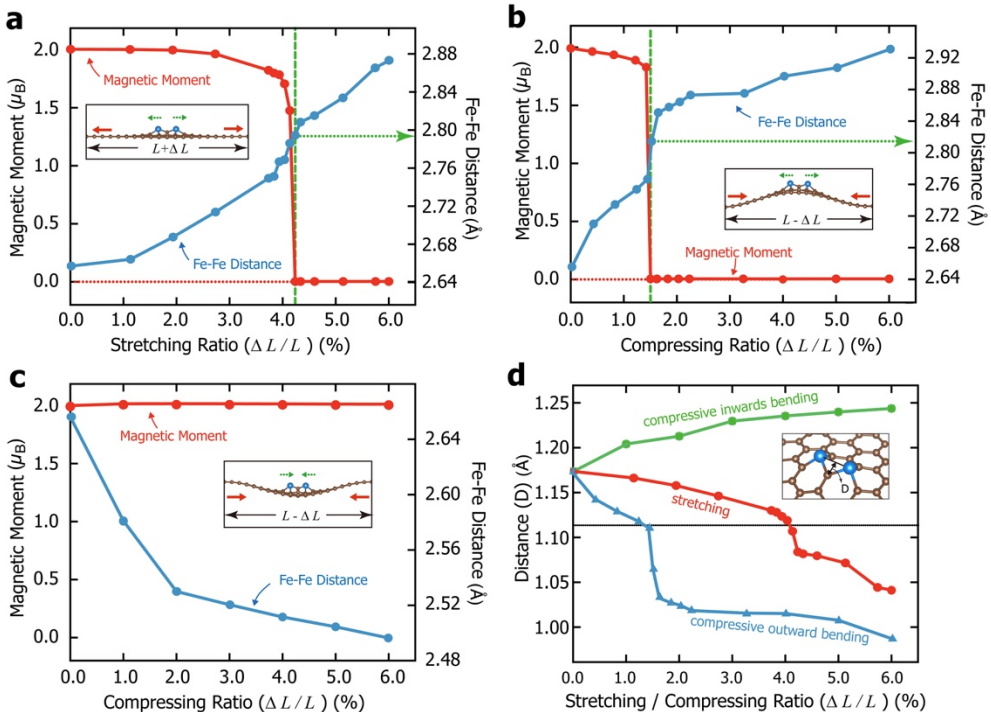

Figure 3.3. Magnetic moment and Fe-Fe distance under the stretching and compressing of graphene. (a) Stretching of graphene, (b) compressive outward bending of graphene, and (c) compressive inwards bending of graphene. (d) Curves of the distance (*D*) from the straight line between two Fe atoms to the carbon atom between two Fe atoms. The inset in (d) shows the distance *D*. The abscissa indicates the stretching or compressing ratio which is given by the rate of change from original size of graphene along *x*-axis. Reprinted with permission from [25]. Copyright 2017 IOP Publishing.

As a counterpart of compressive induced outward bending, the compressive inwards bending is examined in Figure 3.3.c in terms of the changes of magnetic moment and the Fe-Fe distance variations. The magnetic moment remains fairly constant at 2 μ_B for compression ratios up to 6%, indicating that it is very stable. The Fe-Fe distance is reduced to 2.50 Å at the maximum compressing ratio of 6% studied. It has been reported that the value of the magnetic moment for graphene with a single metal atom varies depending on the compression and stretching ratios [28]. However, in our study about the interaction between the two Fe atoms within two vacancies of graphene, the magnetic moment has relatively discrete values of 0 or 2 μ_B for the various compression and stretching ratios. The magnetic moment disappears quickly when the Fe-Fe distance also increases abruptly from 2.74 Å to 2.82 Å in the stretching mode (Figure 3.3.a) and from 2.76 Å to 2.84 Å under the outward bending compression mode (Figure 3.3.b).

At the same time, the distance *D* (Figure 3.3.d inset) from the straight line between the two Fe atoms to a carbon atom in between also decreases abruptly near 1.11 Å, as shown in Figure 3.3.d. The decrease of *D* is closely related to the abrupt increase of the Fe-Fe distance, and it is considered that the carbon atom can have more space to intrude due to the increase of the Fe-Fe distance. It is this intrusion of the carbon atom which quenches the magnetic moment, due to obstruction of the Fe-Fe interaction.

3.3.2. Electronic structure analysis on the interaction between Fe dopants

We analyze the electronic structure to explain the origin of the magnetic moment in the DiFe@2MV. First, we examine the basic case of the electronic structure of the Fe@MV, as it having no magnetic moment is perhaps unexpected, considering that both the ferromagnetic metal atom and the monovacancy are each individually expected to possess a magnetic moment [29].

In order to analyze the magnetic properties of the Fe@MV, we plot the partial density of states (PDOS) in Figure 3.4.a, where the main hybridization is between the Fe *d* state and the dangling bonds states from the neighboring carbon atoms. The coupling between the dangling bond states (D_a and D_e) and the Fe *d* states depends on the symmetries of the states. The structure of the Fe@MV has D_{3h} group and Fe *d* electrons split into three symmetric states, (d_{yz}, d_{zx}), ($d_{x^2-y^2}$, d_{xy}), and d_{z^2} from crystal field theory. The largest coupling occurs between Fe-d_{yz}, d_{zx} and carbon D_e states (Figures 3.4.a and b). Due to the strong Fe-d_{yz}, d_{zx} and D_e coupling, the bonding-antibonding separation of the Fe-d_{yz}, d_{zx} and D_e hybrid states is observed so that the antibonding Fe-d_{yz}, d_{zx}-derived state near 2 eV becomes unoccupied, whereas the bonding Fe-d_{yz}, d_{zx}-derived state near −3 eV is occupied (Figure 3.4.a).

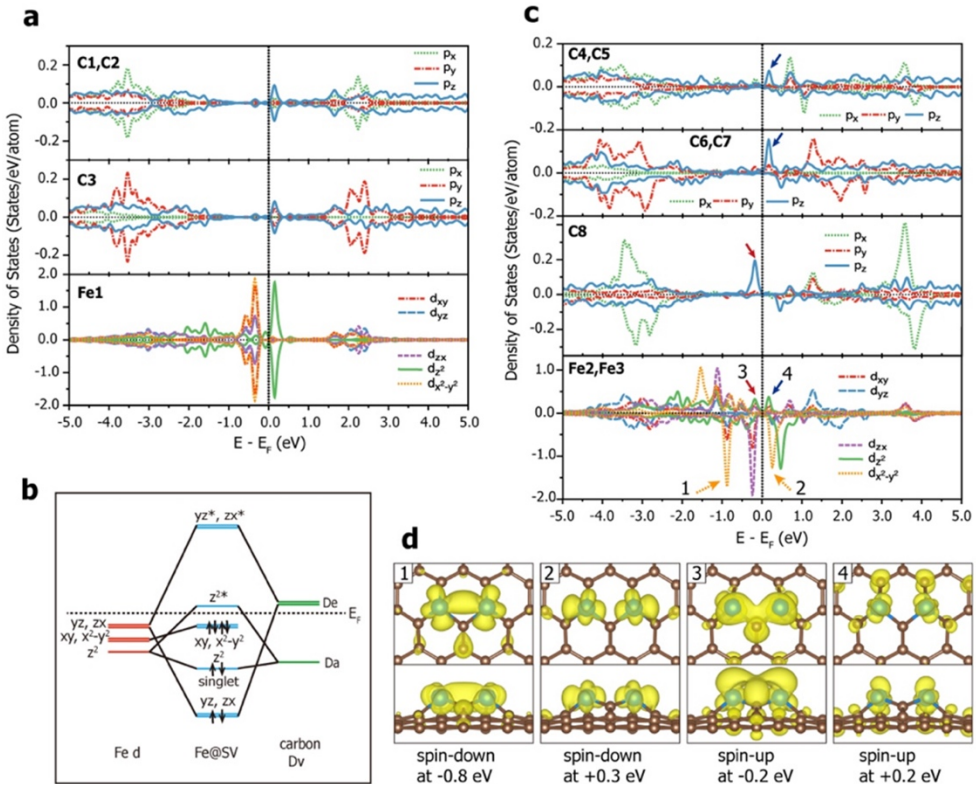

Figure 3.4. Electronic structures of Fe@MV and DiFe@2MV. (a) The PDOS plot and (b) the schematic drawing of energy diagram of Fe@MV. (c) The PDOS plot of DiFe@2MV. (d) The partial spin density plot with an isosurface of 0.0016 e/a_0^3 (a_0 is Bohr radius) for important peaks in PDOS in (c). Alphabets with numbers in each panel of (a) and (c) are corresponding to atoms in structural models of Figure 3.1. The arrows with numbers in (c)-Fe2, Fe3 are corresponding to the partial spin density plots in (d). Reprinted with permission from [25]. Copyright 2017 IOP Publishing.

It is also shown that Fe d_{z^2} couples mostly to a carbon vacancy defect level D_a and it induces the bonding-antibonding separation of Fe-d_{z^2}-derived states. The occupied Fe-d_{z^2}-derived state is considered to be a spin-singlet state (Figure 3.4.b) and the state is broadened from −2 eV to −1 eV (Figure 3.4.a-Fe1). From the PDOS of the Fe@MV, the Fe- $d_{x^2-y^2}$ and d_{xy} are found to be non-bonding states because the electron states of carbon are hardly found at −0.3 eV. The Fermi energy is located right below the Fe d_{z^2} antibonding state. Therefore, one spin-up and one spin-down electron fill the Fe-d_{yz}, d_{zx} states, one electron of spin singlet fills the Fe-d_{z^2} state, and two spin-up and two spin-down electrons fill the Fe-$d_{x^2-y^2}$ and d_{xy} states (Figure 3.4.b). Thus, the total magnetic moment is found to be zero in the Fe@MV.

In Figure 3.4.c, we also plot the PDOS of DiFe@2MV to analyze the origin of the magnetic moment (2 μ_B) and demonstrate that the interaction between two neighboring Fe atoms plays an important role in the generation of the magnetic moment in the DiFe@2MV. The occupied nonbonding $d_{x^2-y^2}$ states in the Fe@MV split into bonding-antibonding states by the Fe-Fe interaction in DiFe@2MV, so that $d_{x^2-y^2}$-derived unoccupied states appears near 0.3 eV in the down-spin d PDOS of DiFe@2MV, whereas the spin-up (↑) $d_{x^2-y^2\uparrow}$ states are broadened from −2 eV to −0.5 eV. The bonding-antibonding splitting of spin-down (↓) $d_{x^2-y^2\downarrow}$ is clearly shown in the isosurface of the spin density in Figures 3.4.d (1) and (2).

Due to the interaction among two Fe atoms and the carbon atom in between within the DiFe@2MV, an antibonding Fe d_{z^2}-carbon D_a hybrid state in the Fe@MV splits and some of it appears below the Fermi energy (red arrows in Figure 3.4.c), which contributes to spin-up states in the DiFe@2MV. This is clearly shown from the change of carbon p_z states into occupied states at −0.2 eV (Figure 3.4.c (C8)). The strong hybridization among two Fe atoms and a carbon atom in between contributes to the occupied spin-up states (Figure 3.4.d (3)), whereas the

hybridization with other neighboring carbon atoms contributes to unoccupied spin-up states (Figure 3.4.d (4)). The generation of a magnetic moment from the change of $d_{x^2-y^2\downarrow}$ and $d_{z^2\uparrow}$ states by the Fe-Fe interaction in the DiFe@2MV is similar to the formation of a magnetic moment by the spin split of e_g electrons in bulk bcc Fe [30].

We have also analyzed the electronic properties of Fe on-graphene system under the stretching or compressive bending of graphene. Until the magnetic moment disappears, the PDOS under the stretching or compressing of graphene is very similar to the PDOS of the DiFe@2MV in Figure 3.4.c. After the magnetic moment disappears, the PDOS becomes very similar to that of the Fe@MV. Figure 3.5.a shows the PDOS of DiFe@2MV at the stretching ratio of 6%. In Figure 3.5.a, the antibonding state of $d_{x^2-y^2\downarrow}$ goes down below the Fermi level to become an occupied state at −0.3 eV. The bonding state of $d_{x^2-y^2\downarrow}$ at −0.7 eV becomes similar to nonbonding states. This is presumably due to the blocking of the bonding configuration between the two Fe atoms by the carbon atom. As mentioned in Figure 3.3.d, when the magnetic moment disappears under stretching or compressive outward bending, the distance *D* decreases abruptly. Hence, the carbon atom intrudes between the two Fe atoms to quench the magnetic moment.

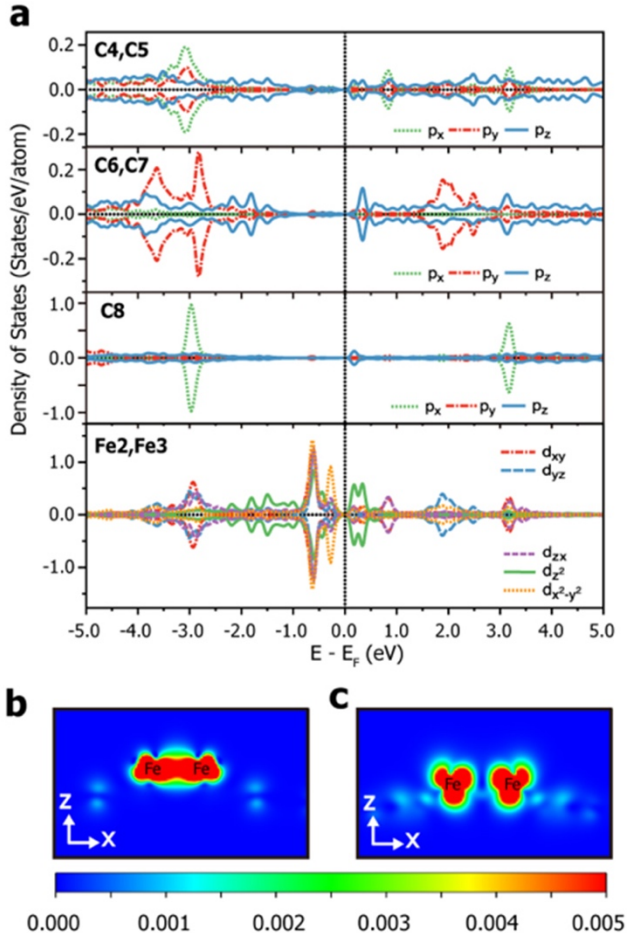

Figure 3.5. The PDOS plot of DiFe@2MV under the stretching ratio of 6% and partial spin density plots. (a) The PDOS plot of DiFe@2MV under the stretching ratio of 6%. (b) Partial spin density plots for spin-down electrons of DiFe@2MV without any strain near −0.8 eV (see arrow 1 in Figure 3.4.c-Fe2, Fe3). (c) Partial spin density plot for spin-down electrons of DiFe@2MV under the stretching ratio of 6% near −0.7 eV in the *xz* plane containing two Fe atoms. The unit of spin density is e/a_0^3 (a_0 is Bohr radius). Reprinted with permission from [25]. Copyright 2017 IOP Publishing.

This becomes evident in Figure 3.5.c with the *xz* plane plot of spin density. Compared to the spin density plot (Figure 3.5.b) near −0.8 eV of DiFe@2MV, the spin density plot (Figure 3.5.c) near −0.7 eV of the system under the stretching of 6% shows an inhibition of the bonding between the two Fe atoms to become similar to the nonbonding state which was found in Fe@MV. In the case of compressive inwards bending, the magnetic moment is invariant at 2 μ_B up to the compressing ratio of 6% and the PDOS is similar to the PDOS (Figure 3.4.c) of DiFe@2MV. In the case of outward bending, the PDOS is similar to that of DiFe@2MV until the compression ratio becomes 1.0%, whereas at a larger compressing ratio than 1.50% the magnetic moment becomes zero and the PDOS becomes similar to that of Fe@MV.

To elucidate the role of the carbon atom in the quenching of the magnetic moment we have also calculated the magnetic moment when moving the carbon atom (C8 in Figure 3.1) along the positive y direction to reduce the distance *D*, while keeping the Fe-Fe distance constant. In the calculation, the magnetic moment is reduced from 2 μ_B and disappears at the distance D = 1.01 Å. Analysis of the electronic structure reveals continuous changes to the electronic structure. As the distance *D* decreases, the typical bonding-antibonding separation of $d_{x^2-y^2\downarrow}$ found in Figure 3.4.c-Fe2, Fe3 gradually disappears, and the unoccupied antibonding state goes down below the Fermi level. We confirm the relevance of *D* for determining the deactivation of the magnetic moment by increasing *D* in the magnetically inactive 6% strained structure. As expected, moving the carbon atom away from the Fe atoms, while keeping the distance between two Fe atoms constant, causes the bonding-antibonding separation of $d_{x^2-y^2\downarrow}$ to be recovered and the magnetic moment to be revived to 2 μ_B at the distance D = 1.27 Å. These results show the key role of the carbon atom in determining the magnetic properties.

3.3.3. Discussion

Magnetic system generally requires dense k-point grid to obtain accurate results. However, since our simulation model has a fairly large unit cell size, we can expect to obtain accurate results even with a relatively small amount of k-points. In Table 3.1, k-point test results for some representative structures are shown. Comparing Γ-point only and 2×2×1 grid, total energy difference of the 6 % stretching case is the largest among representative structures, which is 0.757 eV. This value is very small if we consider the value divided by the number of atoms, that is (0.757 ÷ 200) = 3.79 meV. In addition to this, we used 3×3×1 k-point grid, and the total energy differences between this and 5×5×1 grid are 15 ~ 20 meV. Therefore, our results are very accurate concerning k-point sampling.

Someone may question the relative stability of magnetic ordering of Fe dopants in graphene. Fe dopant pair can have ferromagnetic (FM) or antiferromagnetic (AFM) ordering. Thus, we checked stability of both magnetic orderings for the case without structural deformation ($\mu_B = 2$) and for the case that vanishing of magnetic moments ($\mu_B = 0$) caused by structural deformation. The results are summarized in Table 3.2. For the pristine case, magnetic moment is 2 μ_B and Fe dopants has FM ordering. However, for the stretching and compressive outward bending, AFM ordering becomes more stable than FM ordering and magnetic moment is disappeared. For the pristine case, magnetic moment is 2 μ_B and Fe dopants has FM ordering. However, for the stretching and compressive outward bending, AFM ordering becomes more stable than FM ordering and magnetic moment is disappeared. In all cases, we assumed that Fe dopants remain in FM ordering. Thus, our simulation results do not properly reflect the relative magnetic ordering stability results shown in Table 3.2. Nevertheless, there is no change in the fact that magnetic moment disappears when deformation is applied to graphene. Therefore, our simulation results are still meaningful in terms of the change in magnetic moment induced by structural deformation of the graphene.

Table 3.1. k-point test results for representative structures. For each case, first row is a total energy and second row is a magnetic moment.

	Γ-point	**2×2×1**	**3×3×1**	**4×4×1**	**5×5×1**
Pristine	−1833.548 eV 2.00 μ_B	−1833.834 eV 2.00 μ_B	−1833.788 eV 1.98 μ_B	−1833.806 eV 2.00 μ_B	−1833.804 eV 2.00 μ_B
6% Stretching	−1817.281 eV 0 μ_B	−1818.038 eV 0.02 μ_B	−1818.032 eV 0 μ_B	−1818.018 eV 0 μ_B	−1818.016 eV 0 μ_B
6% Outward bending	−1829.988 eV 0 μ_B	−1830.330 eV 0 μ_B	−1830.290 eV 0 μ_B	−1830.275 eV 0 μ_B	−1830.270 eV 0 μ_B
6% Inward bending	−1829.501 eV 2.00 μ_B	−1829.860 eV 2.00 μ_B	−1829.813 eV 1.99 μ_B	−1829.831 eV 2.00 μ_B	−1829.828 eV 2.00 μ_B

Table 3.2. Stable magnetic ordering for the selected stretching/compressing ratios of structural deformations. Magnetic moment, and energy difference between FM and AFM ordering (E_{FM}-E_{AFM}) when AFM ordering is more stable than FM ordering is also summarized.

Structural Deformation	Stretching/Compressing ratio (%)	Magnetic moment (μ_B)	Stable magnetic ordering	E_{FM}-E_{AFM} (meV/dopant)
Pristine	0	2.00	FM	-
Stretching	4.13 %	1.46	FM	-
	4.23 %	0	AFM	42
	6.00 %	0	AFM	11
Outward bending	1.42 %	1.82	FM	-
	1.50 %	0	AFM	37
	6.00 %	0	AFM	17
Inward bending	6.00 %	2.00	FM	-

In a literature, the on-site energy U effects has been considered for Mn-doped graphene [31] by DFT + U calculations and it was reported that on-site energy U did not affect magnetic moment value although electronic structure was changed. Thus, we do not consider on-site energy U in this study.

If there are the experiments related to our simulation results, it would be interesting. Just a few months after our study was published, IBM research group and their colleagues demonstrated reading and writing of the magnetism of individual Ho atoms on MgO, and showed that they independently retain their magnetic information over many hours [32]. They used scanning tunneling microscope (STM) to read and write the states of Ho atom. To demonstrate independent reading and writing, they built an atomic-scale structure with two Ho bits, to which they write the four possible states and which they read out both magnetoresistively and remotely by electron spin resonance. These results showed the potential of a magnetic memory device using a single atom and imply our Fe-graphene system also can be used as a magnetic memory device at the atomic level.

3.4. Summary

We have studied graphene as a flexible template to control the interaction between metal atoms doped in the lattice. The magnetic moment of a metal atom pair bonded to adjacent graphene vacancies can be controlled by stretching or compressively bending the graphene, changing the interaction between the dopant metal atoms. The presence of a carbon atom and its interaction with the doped magnetic atoms in the vicinity is shown to play an important role in controlling the magnetic switching of the dopant pair. The control of atomic interactions using the flexibility of graphene may open up new opportunities to design systems that couple mechanical deformations with magnetism and find applications for novel nanoelectronic devices. These results can be also applied to the control of the interaction among various atoms or molecules planted in graphene by stretching or compressing it.

3.5. Bibliography

[1] K. S. Novoselov, A. K. Geim, S. V Morozov, D. Jiang, M. I. Katsnelson, I. V. Grigorieva, S. V. Dubonos, and A. A. Firsov, Nature **438**, 197 (2005).

[2] Y. Zhang, Y.-W. Tan, H. L. Stormer, and P. Kim, Nature **438**, 201 (2005).

[3] K. S. Novoselov, Science (80-.). **306**, 666 (2004).

[4] A. K. Geim and K. S. Novoselov, Nat. Mater. **6**, 183 (2007).

[5] S.-K. Lee, B. J. Kim, H. Jang, S. C. Yoon, C. Lee, B. H. Hong, J. A. Rogers, J. H. Cho, and J.-H. Ahn, Nano Lett. **11**, 4642 (2011).

[6] F. Bonaccorso, Z. Sun, T. Hasan, and A. C. Ferrari, Nat. Photonics **4**, 611 (2010).

[7] M. F. El-Kady, V. Strong, S. Dubin, and R. B. Kaner, Science (80-.). **335**, 1326 (2012).

[8] H. Wang, Y. Yang, Y. Liang, J. T. Robinson, Y. Li, A. Jackson, Y. Cui, and H. Dai, Nano Lett. **11**, 2644 (2011).

[9] Y.-W. Son, M. L. Cohen, and S. G. Louie, Nature **444**, 347 (2006).

[10] W. Y. Kim and K. S. Kim, Nat. Nanotechnol. **3**, 408 (2008).

[11] K. S. Kim, Y. Zhao, H. Jang, S. Y. Lee, J. M. Kim, K. S. Kim, J.-H. Ahn, P. Kim, J.-Y. Choi, and B. H. Hong, Nature **457**, 706 (2009).

[12] S. Bae, H. Kim, Y. Lee, X. Xu, J.-S. Park, Y. Zheng, J. Balakrishnan, T. Lei, H. Ri Kim, Y. Il Song, Y.-J. Kim, K. S. Kim, B. Özyilmaz, J.-H. Ahn, B. H. Hong, and S. Iijima, Nat. Nanotechnol. **5**, 574 (2010).

[13] Y. Meng, Y. Zhao, C. Hu, H. Cheng, Y. Hu, Z. Zhang, G. Shi, and L. Qu, Adv. Mater. **25**, 2326 (2013).

[14] O. Cretu, A. V Krasheninnikov, J. A. Rodr\'\iguez-Manzo, L. Sun, R. M. Nieminen, and F. Banhart, Phys. Rev. Lett. **105**, 113 (2010).

[15] A. W. Robertson, B. Montanari, K. He, J. Kim, C. S. Allen, Y. A. Wu, J. Olivier, J. Neethling, N. Harrison, A. I. Kirkland, and J. H. Warner, Nano Lett. **13**, 1468 (2013).

[16] Z. He, K. He, A. W. Robertson, A. I. Kirkland, D. Kim, J. Ihm, E. Yoon, G.-D. Lee, and J. H. Warner, Nano Lett. **14**, 3766 (2014).

[17] J. Zhao, Q. Deng, A. Bachmatiuk, G. Sandeep, A. Popov, J. Eckert, and M. H. Rummeli, Science (80-.). **343**, 1228 (2014).

[18] J. Lee, W. Zhou, S. J. Pennycook, J.-C. Idrobo, and S. T. Pantelides, Nat. Commun. **4**, 1650 (2013).

[19] Z. Yang, L. Yin, J. Lee, W. Ren, H.-M. Cheng, H. Ye, S. T. Pantelides, S. J. Pennycook, and M. F. Chisholm, Angew. Chemie Int. Ed. **53**, 8908 (2014).

[20] L. Zhao, R. He, K. T. Rim, T. Schiros, K. S. Kim, H. Zhou, C. Gutierrez, S. P. Chockalingam, C. J. Arguello, L. Palova, D. Nordlund, M. S. Hybertsen, D. R. Reichman, T. F. Heinz, P. Kim, A. Pinczuk, G. W. Flynn, and A. N. Pasupathy, Science (80-.). **333**, 999 (2011).

[21] D. Wei, Y. Liu, Y. Wang, H. Zhang, L. Huang, and G. Yu, Nano Lett. **9**, 1752 (2009).

[22] A. V Krasheninnikov, P. O. Lehtinen, A. S. Foster, P. Pyykkö, and R. M. Nieminen, Phys. Rev. Lett. **102**, 126807 (2009).

[23] H. Widjaja, M. Altarawneh, and Z.-T. Jiang, Can. J. Phys. **94**, 437 (2016).

[24] Y. Mao, J. Yuan, and J. Zhong, J. Phys. Condens. Matter **20**, 115209 (2008).

[25] S. Lee, D. Kim, A. W. Robertson, E. Yoon, S. Hong, J. Ihm, J. Yu, J. H. Warner, and G.-D. Lee, J. Phys. Condens. Matter **29**, 085001 (2017).

[26] J. P. Perdew, K. Burke, and M. Ernzerhof, Phys. Rev. Lett. **77**, 3865 (1996).

[27] G. Kresse and J. Furthmuller, Phys. Rev. B **54**, 11169 (1996).

[28] B. Huang, J. Yu, and S.-H. Wei, Phys. Rev. B **84**, 075415 (2011).

[29] P. O. Lehtinen, A. S. Foster, Y. Ma, A. V Krasheninnikov, and R. M. Nieminen, Phys. Rev. Lett. **93**, 187202 (2004).

[30] C. S. Wang, R. E. Prange, and V. Korenman, Phys. Rev. B **25**, 5766 (1982).

[31] M. Wu, C. Cao, and J. Z. Jiang, New J. Phys. **12**, 063020 (2010).

[32] F. D. Natterer, K. Yang, W. Paul, P. Willke, T. Choi, T. Greber, A. J. Heinrich, and C. P. Lutz, Nature **543**, 226 (2017).

Chapter 4. Cr and V substitutional dopants in monolayer MoS_2

4.1. Motivation

The size of the point defect is only atomic scale, but it has a large effect on the materials properties. Many researchers are interested in point defects because it sometimes changes the properties of materials dramatically.

The most natural defects are intrinsic defects. W. Zhou *et al*. observed several kind of intrinsic defects in MoS_2 monolayer using ADF-STEM imaging [1]. They observed point defects such as single sulfur vacancy (V_S), disulfur vacancy (V_{S2}), vacancy complex of Mo and nearby three sulfur (V_{MoS3}), vacancy complex of Mo nearby three disulfur pairs (V_{MoS6}), and antisite defects where a Mo atom substituting a S_2 column (Mo_{S2}) or a S_2 column substituting a Mo atom ($S2_{Mo}$).

To understand stability of these kind of point defects, they carried out DFT calculations. DFT optimized structures are well matched with experimental STEM images and formation energy with respect to S chemical potential showed S vacancy is most stable defects. They also investigated electronic structure variation due to point defects and found that defects levels affect conductance of MoS_2.

In addition to intrinsic defects, extrinsic defects in MoS_2 were also studied. As an example, Y.-C. Lin et al. first reported atomic dopants in MoS_2 monolayer [2]. They also used ADF-STEM to image atomic structures of Re and Au dopants and DFT calculations revealed that formation energy of Re and Au dopants and electronic structure variations.

Furthermore, various experimental and theoretical studies on point defects of MoS_2 have been made. In this context, our colleague observed transition metal dopants in MoS_2 using ADF-STEM technique and confirmed its elemental species using EELS (Figure 4.1.) [3].

These transition metal impurities were identified as Cr and V, which are stable under electron irradiation at 60 to 80 kV. Its stability was maintained when incorporated into line defects, and when heated to elevated temperatures. The combined ADF-STEM and EELS differentiated these Cr and V dopants from other similar contrast defect structures, such as 2S self-interstitials at the Mo site, preventing misidentification.

As in the previous studies introduced above, DFT calculations can be performed with experiments to gain a deeper understanding of structural and electronic properties of the defects in MoS_2, which must be done before applications. Then, we performed DFT calculations in order to confirm the energetic favorability of substitutional defects, the charge state of the dopant, and the potential change to the electronic properties of the MoS_2 incurred through the single atom doping.

In the previous research, formation energy of the defects in MoS_2 was calculated but in many cases their charge states were not considered [1,2,4]. It is important to investigate charge states of the defects because it can give useful information, such as equilibrium structures and concentrations, relative stability of the different charge states, and thermodynamic and optical transition levels associated with deep and shallow centers. Thus, we carried out DFT calculations considering possible charge states of the Cr and V substitutional dopants in MoS_2.

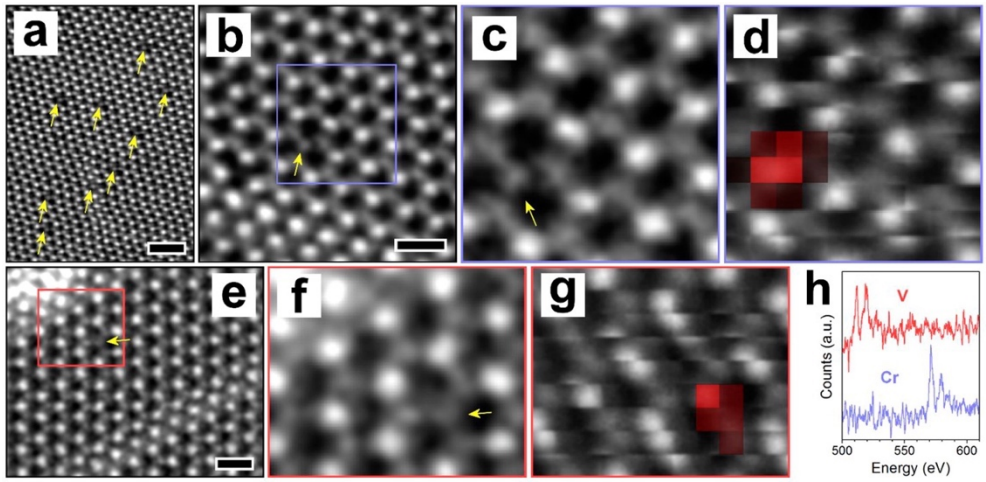

Figure 4.1. ADF-STEM with simultaneous EELS mapping of single atom Cr and V substitution sites (Cr_{Mo} and V_{Mo}). (a) ADF-STEM image of MoS_2 at 300 °C with low contrast single atoms situated at some Mo sites (arrows), in agreement with room temperature experiments. Scale bar corresponds to 1 nm. (b) ADF-STEM image indicating the region for EELS mapping. Scale bar corresponds to 0.5 nm. (c) Magnified ADF-STEM image from the region indicated with the box in (b). (d) Overlay of the integrated EELS intensity (between 570−590 eV) onto the ADF-STEM image acquired at the same time, showing a Cr_{Mo} substitution in the dopant region. Higher red intensity corresponds to greater integrated EELS intensity in the region 570−590 eV for the scanned pixel. (e) ADF-STEM image indicating the region for EELS mapping. Scale bar corresponds to 0.5 nm. (f) Magnified ADF-STEM image from the boxed region in (e). (g) Overlay of the integrated EELS intensity (between 505−525 eV) onto the ADF-STEM image acquired at the same time, showing a V_{Mo} substitution in the dopant region. (h) EELS spectra showing the Cr $L_{3,2}$ and V $L_{3,2}$ edges extracted from the EELS maps in (d) and (g), respectively. Beam accelerating voltage at 60 kV. Reprinted with permission from [3]. Copyright 2016 American Chemical Society.

4.2. Computational details

DFT calculations are carried out to calculate formation energies of the charged dopants Cr_{Mo} and V_{Mo}. The calculations are performed GGA of the PBE functional [5] using VASP code [6]. In the calculation, the basis set contains plane waves up to an energy cutoff of 350 eV, and the structure is relaxed until the force on each atom is smaller than 0.02 eV/Å. The 2 × 2 × 1 grid for k-point is used for the supercell calculations. The in-plane lattice constant of the monolayer MoS_2 is calculated to be a = 3.191 Å and we used this lattice constant as a basic unit length in all directions for the supercell calculations.

The formation energies of the charged defects in neutral and charged states are calculated. The formula of the formation energy is

$$E_{\text{form}} = E_{\text{total}}^{\text{defect}} - E_{\text{total}}^{\text{perfect}} + \mu_{\text{Mo}} - \mu_{\text{X}} + q\left(E_{\text{VBM}}^{\text{perfect}} + E_{\text{Fermi}}\right) + E_{\text{corr}} \quad (4.1)$$

where $E_{\text{total}}^{\text{defect}}$ is the total energy of a monolayer MoS_2 containing Cr (or V) dopants in the $a(6 \times 6 \times 6)$ supercell and $E_{\text{total}}^{\text{perfect}}$ is the total energy of a perfect MoS_2 supercell without a defect. μ_{Mo} is the chemical potential of the Mo and μ_{X} is the chemical potential of the X = Cr, V. These chemical potentials are determined separately in the Mo-rich and the S-rich conditions. In the Mo-rich condition, μ_{Mo} is determined by calculation of the total energy of bulk (bcc) Mo. In the S-rich condition, μ_{Mo} is determined from μ_{MoS_2} that is, total energy of the primitive MoS_2 monolayer and μ_{S} that determined by total energy of the S_8 orthorhombic crystal.

To determine chemical potential of a Cr and V, chemical potentials of all the experimentally known stable binary phases of Cr (or V) and S are calculated because it is hard to directly discern present stable binary phase in the experiments [7,8]. Chemical potentials of the CrS, Cr_7S_8, Cr_5S_6, Cr_3S_4, Cr_2S_3, and Cr_5S_8 (VS_4, V_3S_4,

V_5S_8, V_5S_4, and V_3S for the V-S binary phase) are calculated and the lowest value of μ_{Cr} (or μ_{V}) that can be considered as the most stable phases is selected among each case. q is the charge state of the defect, $E_{\mathrm{VBM}}^{\mathrm{perfect}}$ is the VBM of a monolayer MoS_2 without a defect, and E_{Fermi} is the Fermi level with the reference to the $E_{\mathrm{VBM}}^{\mathrm{perfect}}$. E_{corr} is the energy correction term including the potential alignment and the compensation to the artificial electrostatic energy induced by image charges in supercells for charged defects [9,10].

4.3. Results and discussion

4.3.1. Chemical potential calculations considering binary phases of relevant elements

Chemical potential is the essential state variable for studying the thermodynamics of open systems, in particular chemical reactions, phase transitions, non-uniform systems, surfaces and other cases which can be characterized by varying particle number [11–14]. Chemical potential is a parameter that describes the experimental conditions under which the defect is formed. Therefore, it is important that calculating accurate chemical potential considering the conditions that describe the experimental situation in calculating the defect formation energy.

When Cr and V substitutional dopants are formed in MoS_2, the chemical potentials to be considered are that of Mo, S, Cr, and V. The chemical potentials of Mo and S satisfy simple stoichiometric relation as follows.

$$\mu_{\mathrm{Mo}} + 2 \times \mu_{\mathrm{S}} = \mu_{\mathrm{MoS_2}} \qquad (4.2)$$

The $\mu_{\mathrm{MoS_2}}$ is determined by the DFT total energy of the pristine monolayer of MoS_2 per a formula unit. The chemical potentials of Mo and S are varying between two limit conditions, which are Mo-rich and S-rich conditions. In the Mo-rich condition, μ_{Mo} has the maximum value that same with the DFT total energy of a Mo bcc crystal per an atom and μ_{S} has the minimum value determined by the relation (4.2), and then $\mu_{\mathrm{S}} = (\mu_{\mathrm{MoS_2}} - \mu_{\mathrm{Mo}})/2$.

In the S-rich condition, conversely μ_{S} has the maximum value which corresponds to the total energy of S_8 orthorhombic crystal per an atom and μ_{Mo} is determined by the relation (4.2) reaching to its minimum.

Determining chemical potentials of Cr and V are subtle tricky problem. If experimental situation is not considered, chemical potentials of Cr and V are

determined from the total energy of its bulk form as follows.

$$\mu_{\mathrm{Cr}} = \mu_{\mathrm{Cr}} \text{ (bulk Cr)} \qquad (4.3)$$

$$\mu_V = \mu_V \text{ (bulk V)} \qquad (4.4)$$

However, in the situation that Cr and V substitutional dopants are forming, nobody knows which phases of Cr and V reservoir are involved. Thus, all the possible phases of the reservoir of Cr and V should be considered. Cr and V are not existing as stable chemical compounds with Mo but S can make stable binary compounds with Cr and V. We considered all the possible binary phases of Cr-S and V-S instead of Cr and V bulk.

Experimentally known stable binary phases of Cr-S are CrS, Cr_7S_8, Cr_5S_6, Cr_3S_4, Cr_2S_3, and Cr_5S_8. Assume that Cr reservoir is Cr_3S_4, and then μ_{Mo} and μ_{S} are determined by the relation (4.2) and relevant rich conditions but μ_{Cr} is no longer determined by the total energy of bulk Cr. Now, μ_{Cr} is determined by the stoichiometric relation as follows.

$$3 \times \mu_{\mathrm{Cr}} + 4 \times \mu_{\mathrm{S}} = \mu_{\mathrm{Cr_3}S_4} \qquad (4.5)$$

In this relation, $\mu_{\mathrm{Cr_3}S_4}$ is determined by the total energy of bulk crystal of Cr_3S_4 (C2/m, SG #12) and μ_{Cr} depends on relevant rich conditions. In Mo-rich condition, μ_{S} is determined by relation (4.2) and in S-rich condition μ_{S} has maximum value, which corresponds to the total energy of S_8 crystal. Then, μ_{Cr} is varying between two limit conditions as a function of μ_{S} as follows.

$$\mu_{\mathrm{Cr}} = (\mu_{\mathrm{Cr_3}S_4} - 4 \times \mu_{\mathrm{S}})/3 \qquad (4.6)$$

In this way, μ_{Cr} for other binary phases of Cr-S can be calculated as shown in Figure 4.2. μ_{Cr} calculated using bulk Cr is unchanged even when μ_{S} changes

(black line) but μ_{Cr} calculated using binary phases of Cr-S are depend on the value of μ_S (colored lines).

This approach can be applied to the calculations of μ_V also. The result of μ_V calculations are shown in Figure 4.3. The μ_V were calculated considering experimentally known stable binary phases of V-S, which are VS_4, V_3S_4, V_5S_8, V_5S_4, and V_3S.

Formation energy of Cr_{Mo} and V_{Mo} were calculated using formula (4.1) and we selected the lowest values of μ_{Cr} and μ_V in the Mo- and S-rich limit. These results are summarized in Table 4.1. and 4.2. for the neutral state.

Formation energy of neutral Cr_{Mo} in the Mo-rich limit is 0.75 eV when the μ_{Cr} is calculated from bulk Cr but it becomes 0.54 eV when the μ_{Cr} is selected as the lowest value among the several candidates of Cr-S binary phases. Likewise, formation energy of neutral Cr_{Mo} in the S-rich limit is −1.85 eV when the μ_{Cr} is calculated from bulk Cr but it becomes −0.15 eV when the μ_{Cr} is selected as the lowest value among the several candidates of Cr-S binary phases. Difference between formation energy from bulk Cr and Cr-S binary phases is up to 2.6 eV in the Mo-rich limit. From these results, we can see how important it is to consider possible binary phases of constituent elements.

Formation energy of neutral V_{Mo} also significantly influenced by chemical potential (Table 4.2.). In the Mo-rich limit formation energy of neutral V_{Mo} is 0.28 eV when the μ_V is calculated from bulk V but it becomes 0.89 eV when the μ_V is selected as the lowest value among the several candidates of V-S binary phases. Similarly, formation energy of neutral V_{Mo} in the S-rich limit is −2.33 eV when the μ_V is calculated from bulk V but it becomes 0.42 eV when the μ_V is selected as the lowest value among the several candidates of V-S binary phases

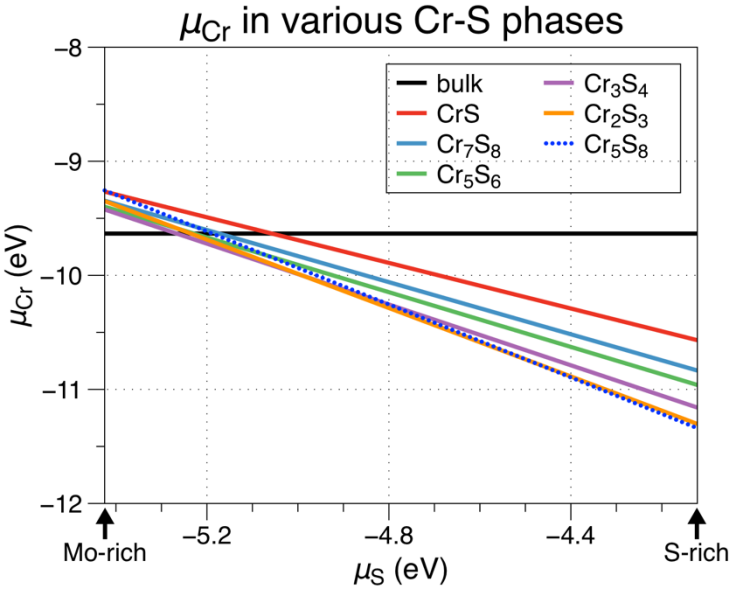

Figure 4.2. The chemical potential of Cr as a function of S chemical potential considering all the possible binary phases of Cr-S.

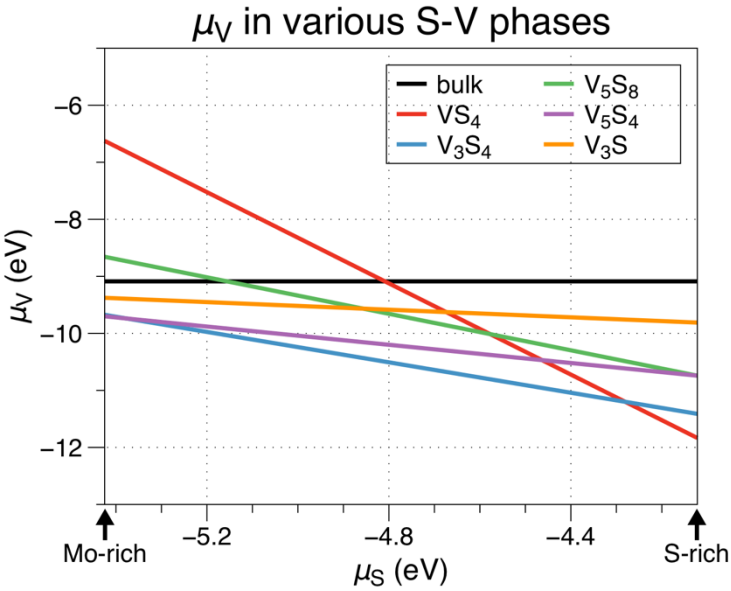

Figure 4.3. The chemical potential of V as a function of S chemical potential considering all the possible binary phases of V-S.

Table 4.1. Difference between formation energies of neutral Cr_{Mo} using bulk Cr and Cr-S binary phases.

	E_{form} (eV)	
	Mo-rich limit	**S-rich limit**
Bulk Cr	0.75	−1.85
Cr-S binary phases	0.54	−0.15

Table 4.2. Difference between formation energies of neutral V_{Mo} using bulk V and V-S binary phases.

	E_{form} (eV)	
	Mo-rich limit	**S-rich limit**
Bulk V	0.28	−2.33
V-S binary phases	0.89	0.42

4.3.2. Stable charge states of Cr and V substitutional dopants and transition level diagram

When formation energy of the defect is calculated considering its charge states, useful information about the defects can be obtained. Thus, formation energy of the Cr_{Mo} and V_{Mo} were calculated for charge states of −2, −1, neutral, +1, and +2. The results are shown in Figure 4.4. and 4.5.

Figure 4.4. is the transition level diagram of Cr_{Mo} and it also shows formation energy of Cr_{Mo} for each charge state in the Mo-rich limit (Figure 4.4.A) and S-rich limit (Figure 4.4.B). In both Mo- and S-rich limit conditions, Cr_{Mo} is found to be stable when it is electrically neutral. The reason why Cr_{Mo} possess neutral state is that the number of valence electron of Cr is same with that of Mo, so Cr_{Mo} can be expected to form similar chemical bonds with the neighboring S atoms. Formation energy of the neutral Cr_{Mo} is 0.54 eV in the Mo-rich limit and −0.15 eV in the S-rich limit.

Likewise, Figure 4.5. shows the transition level and formation energy of V_{Mo} for each charge state in the Mo-rich limit (Figure 4.5.A) and S-rich limit (Figure 4.5.B). V_{Mo} is found to be stable in neutral and −1 charge state and the transition level between these charge states is found to be at the 0.54 eV above the VBM. This result suggests that V_{Mo} may act as a deep single donor in monolayer MoS_2.

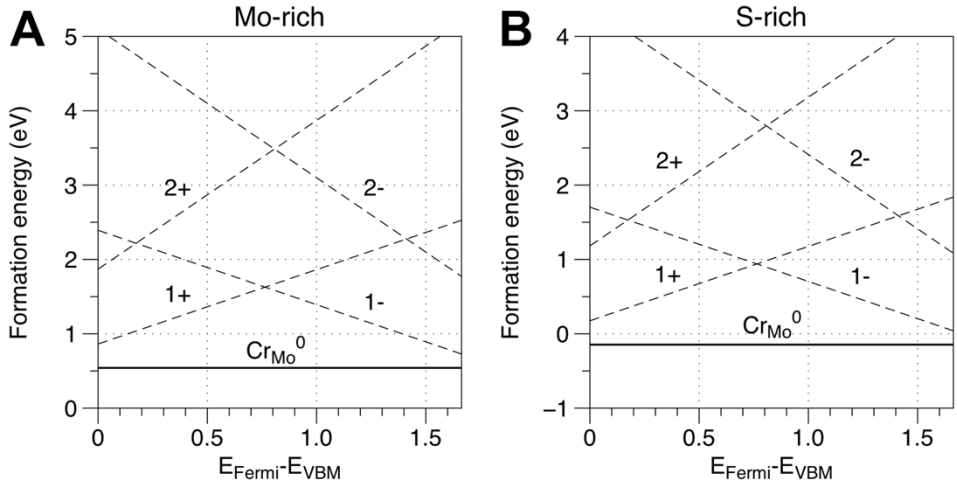

Figure 4.4. Formation energy of Cr_{Mo} in the (A) Mo-rich limit and (B) S-rich limit.

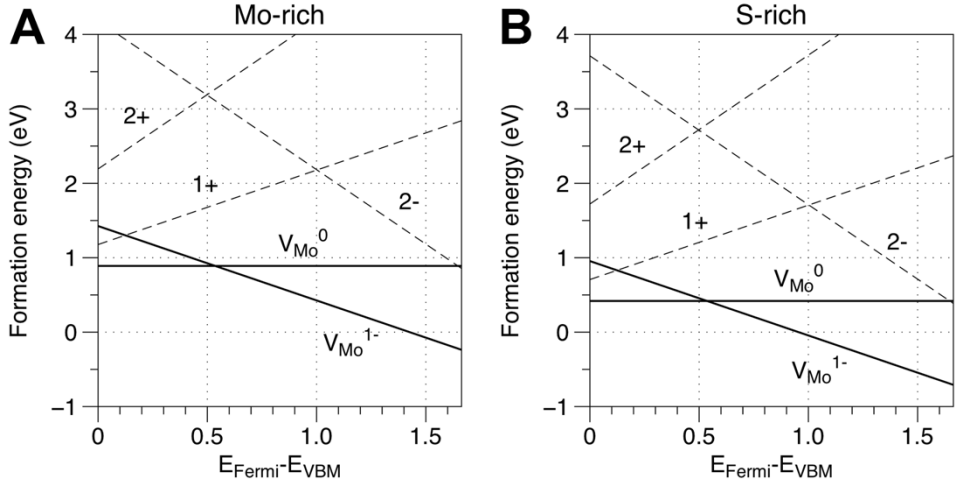

Figure 4.5. Formation energy of V_{Mo} in the (A) Mo-rich limit and (B) S-rich limit.

4.3.3. Density of states analysis of stable charge states of Cr and V substitutional dopants

The electronic density of states (DOS) of Cr_{Mo} and V_{Mo} were calculated for the charge neutral states, and also for the −1 charge state for the case of V, shown in Figure 4.6. The charge neutral Cr_{Mo}, Figure 4.6.B, shows a new low energy peak in the DOS compared to that of pristine MoS_2, Figure 4.6.A, indicating doping of the MoS_2 by the presence of the Cr. Neutral V_{Mo} (Figure 4.6.C) exhibits a local magnetic moment of 1 μ_B generated by the V dopant and its bonding with its neighbor S atoms, yielding a state in the band gap, in agreement with previous calculations [15]. However, the DOS for −1 charged V shows no moment due to the filling of the unpaired valence electrons. The DOS of the −1 charged V_{Mo}, Figure 4.6.D, also shows new low energy peak compared to pristine MoS_2 DOS, confirming it can dope the material.

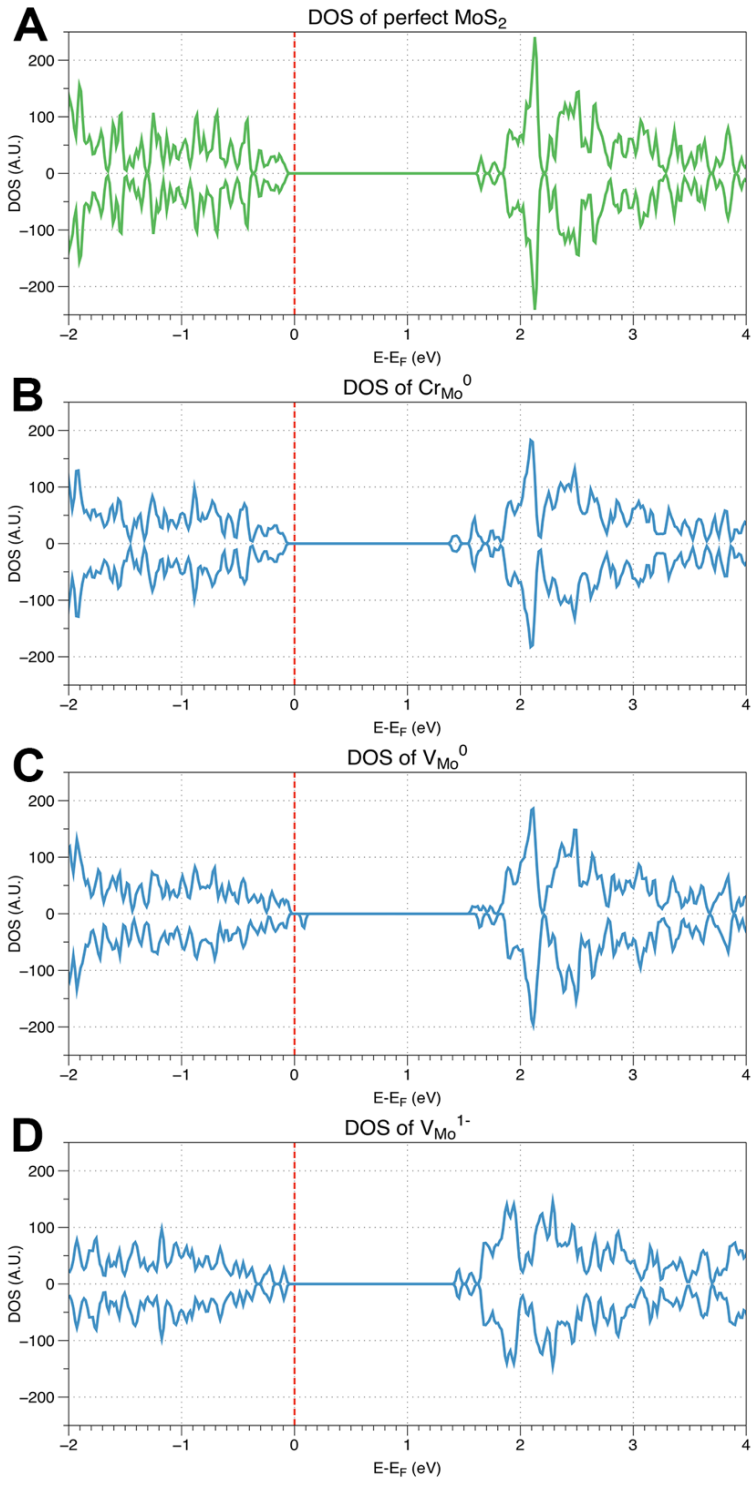

Figure 4.6. Density of states of the (A) pristine monolayer MoS_2, (B) in the presence of neutral Cr_{Mo}, (C) neutral V_{Mo}, and (D) −1 charged V_{Mo}. Fermi level is set to 0 (Red dashed lines). Reprinted with permission from [3]. Copyright 2016 American Chemical Society.

4.3.4. Discussion

There are many efforts to replace conventional Si-based electronic devices using 2D materials such as graphene and TMDs [16–19]. Generally, doping is one of the main approaches has been used to improve the carrier mobility and electrical conductivity of materials used for electronic devices. However, according to our results described above, Cr and V substitutional dopants cannot improve electrical conductivity of MoS_2 because they are either electrically neutral or single deep acceptor.

So, naturally, we can think about how the different kinds of elements affect the properties of MoS_2. Theoretical studies on this subject already have been carried out [4,15,20,21]. J.-Y. Noh *et al*. calculated transition levels of Re and Nb dopants in monolayer MoS_2 [21]. They showed that the Re and Nb dopants are deep level defects in free-standing monolayer MoS_2, like as our results. However, the main point of their report is dielectric environment can alter the situation. They investigated monolayer MoS_2 placed on a (SiO_2 or HfO_2) substrate and/or below an (SiO_2 or HfO_2) encapsulation. The meaning of the abbreviations for the models used in their report are vacuum-MoS_2-vacuum (VMV), vacuum-MoS_2-SiO_2 (VMS), SiO_2 -MoS_2- SiO_2 (SMS), vacuum-MoS_2-HfO_2 (HMH), HfO_2-MoS_2-SiO_2 (HMS), HfO_2-MoS_2-HfO_2 (HMH), respectively. They found that the defect transition levels can shoal with increasing the environmental dielectric constants. They reported the screened Coulomb interaction between the bound electron and the charged impurity induces the deep-to-shallow level transition in monolayer MoS_2 with the dielectric environments.

Therefore, we expect that Cr and V dopants also can be exhibit shallow nature if dielectric environments are considered. In the real situations, dielectric substrate and/or encapsulation environments are essential part of the electronic devices so future work considering dielectric environments is needed for practical novel electronic devices applications using MoS_2.

4.4. Summary

Point defects and impurities often play a decisive role in the physical properties of materials and DFT calculations have emerged as a powerful approach that complements experiments and has become reliable enough to serve as a predictive tool.

We calculated formation energies of Cr and V substitutional dopants in monolayer MoS_2 considering its charge states. Suitable finite size supercell correction scheme was used to compensate spurious electrostatic interaction between image charges. All the possible binary phases of Cr-S and V-S were considered to explore different experimental scenarios.

Cr_{Mo} is stable as electrically neutral and V_{Mo} is stable as neutral and −1 charged state. The (0/−1) transition level of V_{Mo} is 0.54 eV that indicates V_{Mo} acts as a single deep acceptor. Moreover, we found that neutral V_{Mo} shows local magnetic moment of 1 μ_B through the analysis of electronic density of states.

Our results inform that Cr and V substitutional dopants are not useful to enhance electric conductivity of MoS_2. However, it is only the case of free-standing MoS_2, and the fact that dielectric environment may change deep nature of the extrinsic dopant into the shallow nature motivates future work that may change properties of the Cr and V substitutional dopants in dielectric environment.

4.5. Bibliography

[1] W. Zhou, X. Zou, S. Najmaei, Z. Liu, Y. Shi, J. Kong, J. Lou, P. M. Ajayan, B. I. Yakobson, and J.-C. Idrobo, Nano Lett. **13**, 2615 (2013).

[2] Y.-C. Lin, D. O. Dumcenco, H.-P. Komsa, Y. Niimi, A. V Krasheninnikov, Y.-S. Huang, and K. Suenaga, Adv. Mater. **26**, 2857 (2014).

[3] A. W. Robertson, Y.-C. Lin, S. Wang, H. Sawada, C. S. Allen, Q. Chen, S. Lee, G.-D. Lee, J. Lee, S. Han, E. Yoon, A. I. Kirkland, H. Kim, K. Suenaga, and J. H. Warner, ACS Nano **10**, 10227 (2016).

[4] K. Dolui, I. Rungger, C. Das Pemmaraju, and S. Sanvito, Phys. Rev. B **88**, 75420 (2013).

[5] J. P. Perdew, K. Burke, and M. Ernzerhof, Phys. Rev. Lett. **77**, 3865 (1996).

[6] G. Kresse and J. Furthmuller, Phys. Rev. B **54**, 11169 (1996).

[7] B. Predel, in *Cr-Cs – Cu-Zr* (Springer-Verlag, Berlin/Heidelberg, 1994), pp. 1–6.

[8] B. Predel, in *Pu-Re – Zn-Zr* (Springer-Verlag, Berlin/Heidelberg, 1998), pp. 1–3.

[9] H.-P. Komsa and A. Pasquarello, Phys. Rev. Lett. **110**, 095505 (2013).

[10] J.-Y. Noh, H. Kim, and Y.-S. Kim, Phys. Rev. B **89**, 205417 (2014).

[11] T. A. Kaplan, J. Stat. Phys. **122**, 1237 (2006).

[12] G. Job and F. Herrmann, Eur. J. Phys. **27**, 353 (2006).

[13] R. Baierlein, Am. J. Phys. **69**, 423 (2002).

[14] G. Cook and R. H. Dickerson, Am. J. Phys. **63**, 737 (1995).

[15] Q. Yue, S. Chang, S. Qin, and J. Li, Phys. Lett. A **377**, 1362 (2013).

[16] Q. H. Wang, K. Kalantar-Zadeh, A. Kis, J. N. Coleman, and M. S. Strano, Nat. Nanotechnol. **7**, 699 (2012).

[17] K. F. Mak, C. Lee, J. Hone, J. Shan, and T. F. Heinz, Phys. Rev. Lett. (2010).

[18] F. Bonaccorso, Z. Sun, T. Hasan, and A. C. Ferrari, Nat. Photonics **4**, 611 (2010).

[19] O. V. Yazyev and S. G. Louie, Nat. Mater. **9**, 806 (2010).

[20] A. Carvalho and A. H. C. Neto, Phys. Rev. B **89**, 081406 (2014).

[21] J. Noh, H. Kim, M. Park, and Y. Kim, Phys. Rev. B **92**, 115431 (2015).

Chapter 5. S vacancy induced structural phase transition of MoS_2 nanocrystals

5.1. Motivation

Since the first isolation of graphene in 2004 [1,2], two-dimensional (2D) materials such as hexagonal boron nitride (h-BN) [3–5], transition metal dichalcogenides (TMDs) [6–8], and layered metal oxides (LMOs) [9–11] have drawn researchers to examine their unique and exotic properties. Molybdenum disulfide (MoS_2) is a one of the most fascinating materials in this field, and it already has been used as a hydrodesulfurization (HDS) reaction catalyst to remove sulfur from fossil fuels for a several decades [12–14]. Recently, MoS_2 has attracted considerable attention as a hydrogen evolution reaction (HER) catalyst [15–18]. Stable and inexpensive hydrogen production is a prerequisite to use hydrogen as future energy sources. Well-known HER catalysts, platinum and other noble metals, ought to be replaced with earth-abundant and cheap catalysts to smooth the way for hydrogen economy.

Polymorphism is the one of the interesting features of MoS_2 (Figure 5.1). Sulfur atom coordination determine its polytype, termed as 2H, 1T, and 1T' phases. Sulfur atoms are arranged in trigonal prismatic (D_{3h}) symmetry for 2H phase (Figure 5.1.a) and for 1T (Figure 5.1.b) and 1T' (Figure 5.1.c) phases, sulfur atoms are arranged in octahedral (O_h) and distorted octahedral symmetries, correspondingly. Structural differences deviate electronic properties of MoS_2. 2H phase shows semiconducting property, though 1T/1T' phase shows metallic nature. Catalytic efficiency also depends on the structure of MoS_2. Catalytic efficiency of 2H phase is governed by the number of active edge sites because edge sites have metallic edge states. However, limited number of active edge sites and catalytically inactive basal plane are critical problem to maximize catalytic performance of MoS_2. Contrary to 2H phase, 1T phase has both catalytically active basal plane and edges, along with large

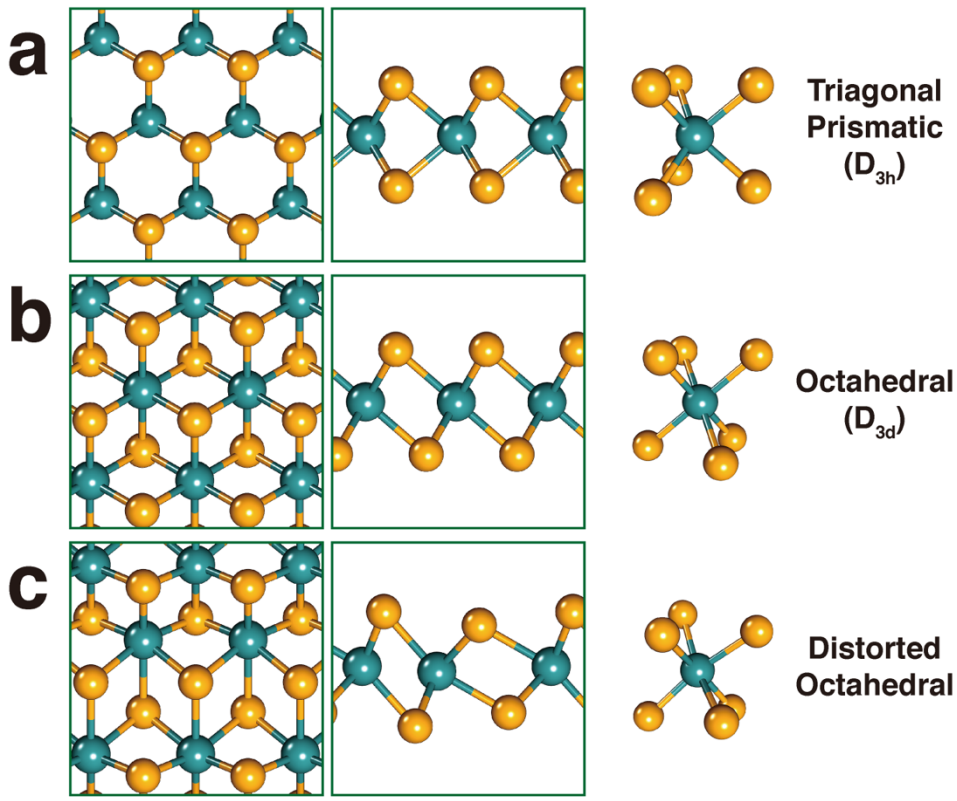

Figure 5.1. Polymorphism of MoS2. Each row shows top view, side view, and crystallographic unit of (a) 2H, (b) 1T, and (c) 1T' phases.

electric conductance. Bulk MoS_2 is naturally found as 2H phase, which is thermodynamically more stable than 1T phase. Thus, various methods have been suggested to synthesize 1T phase to examine its HER efficiency. Li intercalation methods were predominantly used to obtained chemically exfoliated metallic nanosheets of 1T phase MoS_2 [19,20]. Substitutional Re doping [21], strain engineering [22,23], electron irradiation [24], and charge injection [25] were reported to cause phase transition from 2H to 1T. In the theoretical aspect, Enyashin *et al.* and Kan *et al.* carried density functional theory (DFT) calculations of structures and stability of Li adsorbed MoS_2 system [21,26,27]. Gao *et al.* reported detailed processes of phase transition and HER activity of 1T/1T' phase MoS_2 by DFT calculations and they showed negative charge plays important role in phase transition [28]. Sun *et al.* also reported that charge transfer from intercalated alkali metals is the starting point in phase transition [29].

In this chapter, we report novel and simple method of phase transition from 2H to 1T phase and carbon monoxide (CO) molecules are effective initiator of phase transition, especially for triangular MoS_2 nanocrystals. Our colleagues recently reported the experimental results that MoS_2 nanocrystals synthesized in carbon nanofiber transform from 2H to 1T phase after CO gas annealing at 800 ℃. The size of MoS_2 nanocrystals synthesized in carbon nanofiber is about 5 nm and few layers are stacked. They also reported COS gas was detected during the annealing and S vacancies exist up to 25% less than standard stoichiometry of MoS_2. From these results, we could guess that CO molecules bind with S in MoS_2 nanocrystals and S vacancies are produced along with COS gas. We expected that S vacancies play an important role in this structural phase transition, so we tried to explain detailed atomic-scale mechanism of phase transition and stability of 1T-MoS_2 using DFT calculations

Related studies already have been carried out. Zan *et al.* reported phase crossover of transition metal dichalcogenide nanoclusters [31]. They reported the

stability of MX_2 (M = Mo, W; X = S) clusters with different phases and morphologies. Surprisingly, the MX_2 clusters exhibit a high level of phase variability, varying from the H phase, favorable in the 2D extended form, to the T phase at a smaller cluster size or lower chemical potential of X. They also constructed a novel phase diagram by expressing the total energy of various clusters as a function of the chemical potential and cluster size. However, they did not consider the role of S vacancy and detailed atomic-scale mechanism of phase transitions.

Bruix *et al.* reported that how cluster size and interaction with a metal surface affect the stability and properties of different MoS_2 clusters and the resulting phase diagrams [32]. They also demonstrated that interaction with Au(111) substrate modifies the relative stability of the different nanocluster types so that edge terminations and crystallographic phases that are metastable for free-standing nanoclusters and monolayers are expressed in the supported systems. Nevertheless, they did not investigate atom-scale mechanism of phase transition. The difference between previous studies and our report is that we aimed to reveal an atomic-scale mechanism of structural phase transition of MoS_2 nanocrystals.

Lauritsen *et al.* reported structural characters of triangular MoS_2 nanocrystals as a function of their size using atom-resolved scanning tunneling microscope (STM) [33]. They observed two different edge terminations of MoS_2 nanocrystal, which is $(10\bar{1}0)$ Mo and $(\bar{1}010)$ S edges and each edge terminations can be covered with varying coverage of sulfur atoms. Considering both the crystallographic direction and the S coverage, the type of edge most observed varies depending on the size of MoS_2 nanocrystals. The size of MoS_2 nanocrystals was defined as a number n of Mo atoms at the side of the triangle and $n = 6$ is the border where the type of edge termination changes from Mo edge (100% S coverage) to S edge (100% S coverage). Therefore, we performed DFT calculations for MoS_2 nanocrystals of size $n = 6$ to take all possible cases into account.

5.2. Computational details

We performed DFT calculations within the generalized gradient approximation (GGA) of the Perdew−Burke−Ernzerhof (PBE) functional [34] using Vienna ab initio simulation package (VASP) code [35]. The orthorhombic unit cell containing n = 6 triangular S-edge MoS_2 nanocrystals (100% S coverage) was constructed including a vacuum region of > 20 Å in all directions to prevent interactions between periodic images. Detailed explanations to terminology and atomic structure of triangular MoS_2 nanocrystals can be found in Ref. [33]. The basis set contained plane waves up to an energy cutoff of 400 eV. The Brillouin zone was sampled using a 2×2×1 Monkhorst-Pack mesh. For structural optimization, all atomic positions were fully relaxed until the force on each atom was smaller than 0.02 eV/Å. To obtain activation barrier of each reactions, we implemented constraint structure optimization scheme to the original VASP code.

.

5.3. Results and discussion

5.3.1. Edge S coverage dependent structural stability of MoS_2 nanocrystals

First, we examined structural stability of triangular MoS_2 nanocrystals with respect to the edge S coverage. We investigated structural stability of size $n = 6$ and S edge termination with varying S coverage of 100%, 75%, 50% (Figure 5.2.). We intentionally removed edge S atoms to construct 2H and 1T phases for each case and then performed structural optimization to compare the total energy between 2H and 1T phases. Here, we could find that there are two types of structures when S coverage is 75%, which we termed type1 and type2.

When the S coverage is 100%, it is confirmed that the 2H phase is more stable than the 1T phase, as previously reported. However, when S coverage is 75% and 50%, it is confirmed that 1T phase is more stable than 2H phase. In the case of type 1, 75% S coverage, the energy difference between 2H phase and 1T is greatest and there was no tendency to increase the energy difference between the 2H phase and 1T phase as the S coverage decreased. However, it is clear that the 1T phase is stabilized with S deficient edge. From these results, we have found that the removal of S atoms by CO gas is thermodynamically feasible enough to cause a transition from 2H to 1T phase.

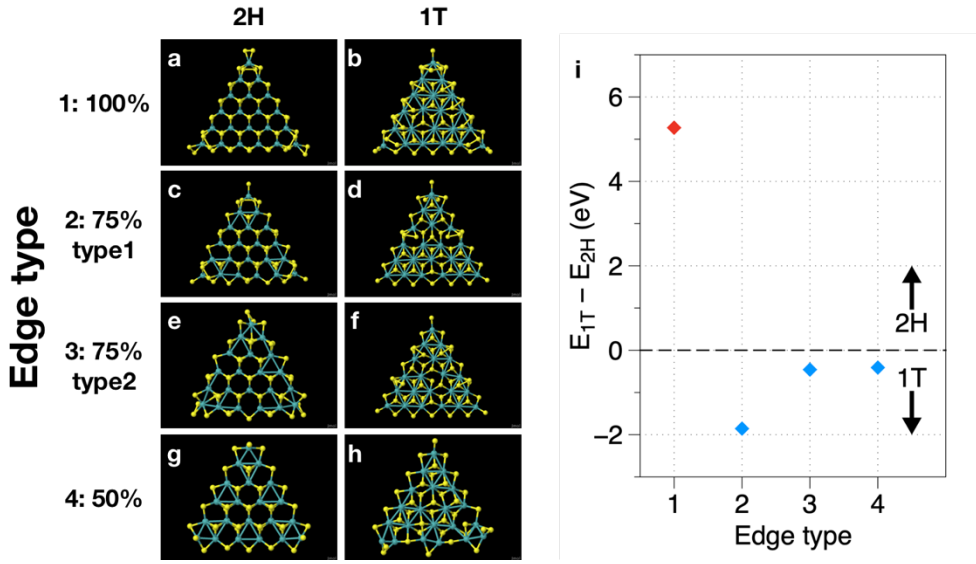

Figure 5.2. Structural stability of $n = 6$ triangular MoS_2 nanocrystals. Atomic model of DFT optimized 2H and 1T phases for the (a, b) 100% S coverage, (c, d) type 1, 75% S coverage, (e, f) type 2, 75% S coverage, (g, h) 50% S coverage. (i) Total energy differences between 2H and 1T phases for each edge type shown in panel a-h.

5.3.2. Detailed atomic-scale mechanism of phase transition of triangular MoS_2 nanocrystals

For the next step, we investigated the detailed atomic-scale mechanism of the structural phase transition of triangular MoS_2 nanocrystals from 2H to 1T. First, we checked that at which site S atoms are most easily removed (Figure 5.3.). There are three candidates, where S atoms can be removed, which are vertex, edge, and surface (basal plane). We calculated total energy for each step that CO molecule approaches to the S atom and bind with it to form COS molecule and S vacancy. At the surface, reaction barrier is 2.24 eV that indicates S atom at the surface is hard to be removed by CO gas. However, at the edge and vertex of MoS_2 nanocrystal, S atom easily desorbed by CO gas. Reaction barriers for the edge case is 0.07 eV and surprisingly reaction can be occurred without barrier at the vertex. From this result, we could confirm that the removal of the S atom from the surface would be more difficult than removing it at the vertex or edge. Therefore, we set vertices and edges, especially vertices, as the starting point for S atom removal by CO gas.

We have performed a reaction barrier calculation for a detailed atomic-scale phase transition mechanism starting from the removal of the S atom at the vertex and edge. We did not calculate whole phase transition process until MoS_2 nanocrystal transforms into 1T phase completely but calculated initial part of phase transition because of limit of computational resources. Nevertheless, we could confirm that phase transition from 2H to 1T is thermodynamically favorable and give reasonable explanation for the atomic-scale mechanism of phase transition.

DFT calculated energy diagram for the stepwise reactions shown in Figure 5.4. and atomic models for each step are shown in Figure 5.5. At first, S atom at vertex (green arrow in panel 1 of Figure 5.5.) desorbed by CO molecule. In Figure 5.5, TS means transition state. As mentioned above, there is no reaction barrier for the step from 1 to 2, then S atom is desorbed, and S vacancy is formed at vertex. Optimized structure after S atom at vertex was desorbed is shown in panel 2 of Figure 5.5. Total

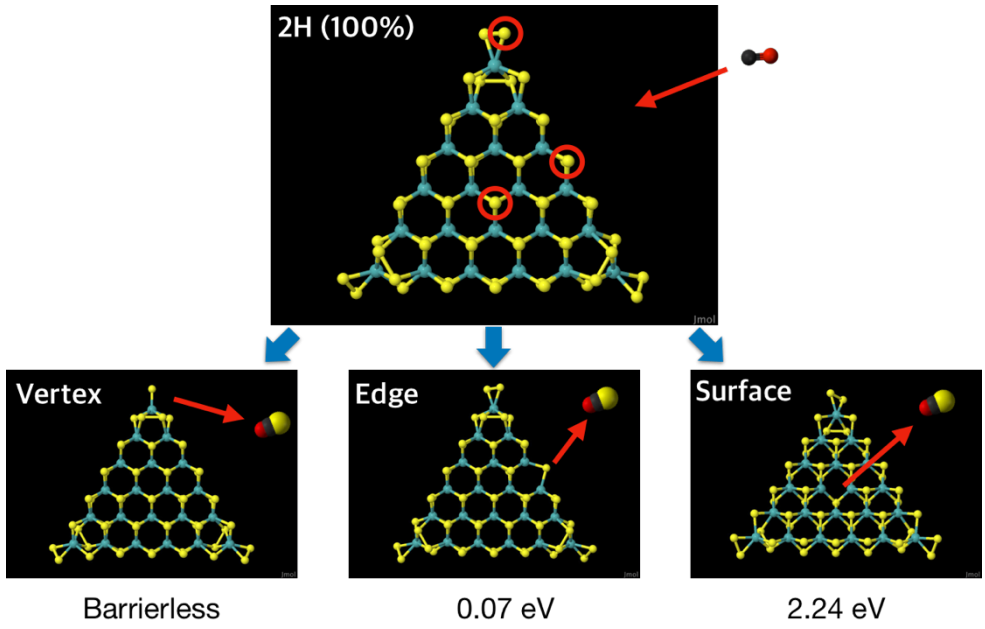

Figure 5.3. Reaction barriers for S removal at vertex, edge, and surface by CO gas. (Upper panel) S atom at each site (red circles) can be desorbed from 2H, 100% S coverage MoS_2 nanocrystal by CO gas. (Lowe panels) Atomic model for the DFT optimized structures after S atom at vertex, edge, and surface form COS molecule. Reaction barriers for each case are barrierless, 0.07, and 2.24 eV, respectively.

energy of state 2 is −0.76 eV lower than that of state 1, that indicate this reaction is thermodynamically favorable.

For the next step, two S atoms (green and red arrow in panel 2 of Figure 5.5.) at the edge site nearly next to the vertex can be desorbed. We calculated both cases that S atom at upper side and at lower side is desorbed. For lower side S atom, reaction barrier is 0.99 eV and for upper side S atom 1.64 eV. These values are presented in energy diagram (Figure 5.4.) also. For the clear understanding, in Figure 5.4. and 5.5, if there are two paths to a certain reaction, the one with the higher reaction barrier is marked in red and the one with the lower reaction barrier is marked in green.

After S atom at edge is desorbed, we calculated reaction barrier that S atom at other edge site migrates (direction of sky-blue arrow in panel 3 in Figure 5.5.) to the hollow site of Mo-S hexagon (green arrow in panel 3 of Figure 5.5.). Migration barrier of this reaction is calculated to be 0.11 eV and optimized structure of final state is shown in panel 4 of Figure 5.5. Interestingly, migrated S atom made bond with three Mo atoms and local structure nearby migrated S atom is changed to 1T phase.

Setting state 4 as an initial state, we calculated reaction barrier of desorption of the S atom at another edge (panel 4 of Figure 5.5.). CO molecule is bonded with S atom at lower side (red arrow) spontaneously, and then S atom is desorbed with 0.13 eV reaction barrier. However, S atom at upper side is desorbed without barrier.

After S atom desorption, we calculated reaction barrier that S atom at surface (green arrow in panel 5 of Figure 5.5.) migrates to another hollow site (direction of sky-blue arrow). The calculated reaction barrier for this process is 0.52 eV, which is slightly larger than the migration barrier 0.11 eV in the previous step 3-4. After migration is finished, local structure around migrated S atom changes into 1T phase once more (panel 6 of Figure 5.5.).

In the process from state 6 to 8, S atom desorption occurs in a slightly different

manner from the case described above. The S atom at the lower side, the CO molecule is first adsorbed to the S atom (panel 7 of Figure 5.5.) before the S atom is desorbed, and this adsorption process is barrierless. The process of forming S vacancy along with desorption of COS molecule is also barrierless. In the case of the S atom at the upper side, CO molecule adsorbed first as in the case of S atom at the lower side. In this process, reaction barrier of CO adsorption is 0.21 eV. The reaction barrier of the subsequent desorption of the S atom has a small value of 0.07 eV.

As the last step of our calculations, two S atom at fourth edge site are desorbed to form state 9. The reaction barriers for upper and lower S atom are 0.58 and 0.48 eV, respectively.

We did not perform calculations for the whole process that MoS_2 nanocrystal transforms to the 1T phase, but in general, each state shown above were transformed into lower energy states. Our results suggest that the processes we calculated are thermodynamically favorable.

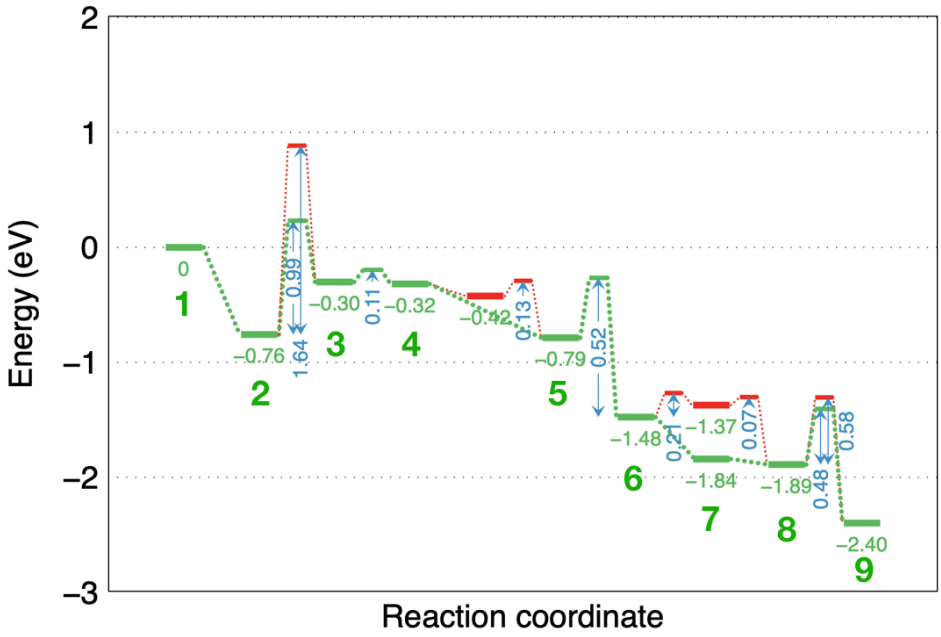

Figure 5.4. Energy diagram for the stepwise reactions during phase transition of MoS_2 nanocrystal.

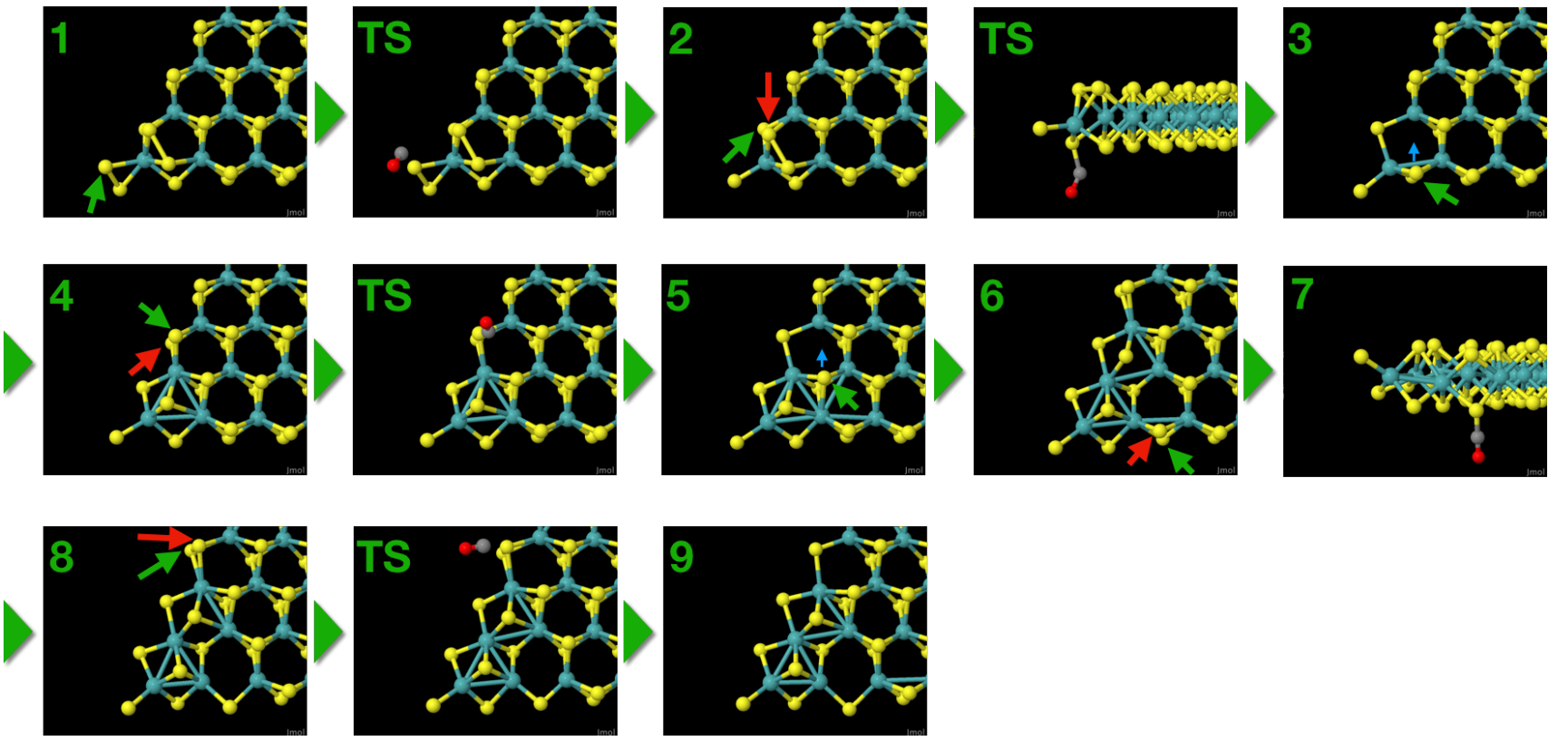

Figure 5.5. Atomic model for each reaction corresponds to the energy diagram shown in Figure 5.4.

5.3.3. Discussion

The results of the above calculations are summarized as follows.

- S vacancies are easily formed at the vertices and edges by the CO molecules.
- S atoms on the surface easily migrate to the hollow site of hexagon where around S vacancy is formed.
- The local structure of MoS_2 nanocrystals gradually changes to 1T phase due to S vacancy formation at vertex and edge and S atom migration on the surface.

Our results suggest that MoS_2 nanocrystal of larger edge/surface ratio, *i.e.*, smaller size MoS_2 nanocrystal can be easily transformed to the 1T phase. The experimental results also support our hypothesis. About 50% of the ~ 5 nm sized nanocrystals inside the carbon nanofiber changed to 1T phase, but when the same experiment was performed on the micrometer sized commercial power sample, only 5~10 % was changed to1T phase.

Since we performed calculations only for MoS_2 nanocrystals with S edge termination, someone may have questions about what happens in the case of the Mo edge termination mentioned above. In the case of Mo edge, transition to 1T phase also can be explained according to our hypothesis without detailed reaction barrier calculations (Figure 5.6.). DFT optimized structure of the Mo edge nanocrystal is shown in Figure 5.6.a. In the case of Mo edge nanocrystals, we can infer that CO molecules can easily bind with S atoms at the vertices and edges to form S vacancies. Moreover, we can infer that S atoms on the surface of nanocrystal can easily migrate to another site. If these reactions continue, the local structure of the Mo edge nanocrystals will gradually change to 1T phase. We cannot know exactly what the final structure of the Mo edge nanocrystal will be, but it can be explained that the entire system will be thermodynamically more stable.

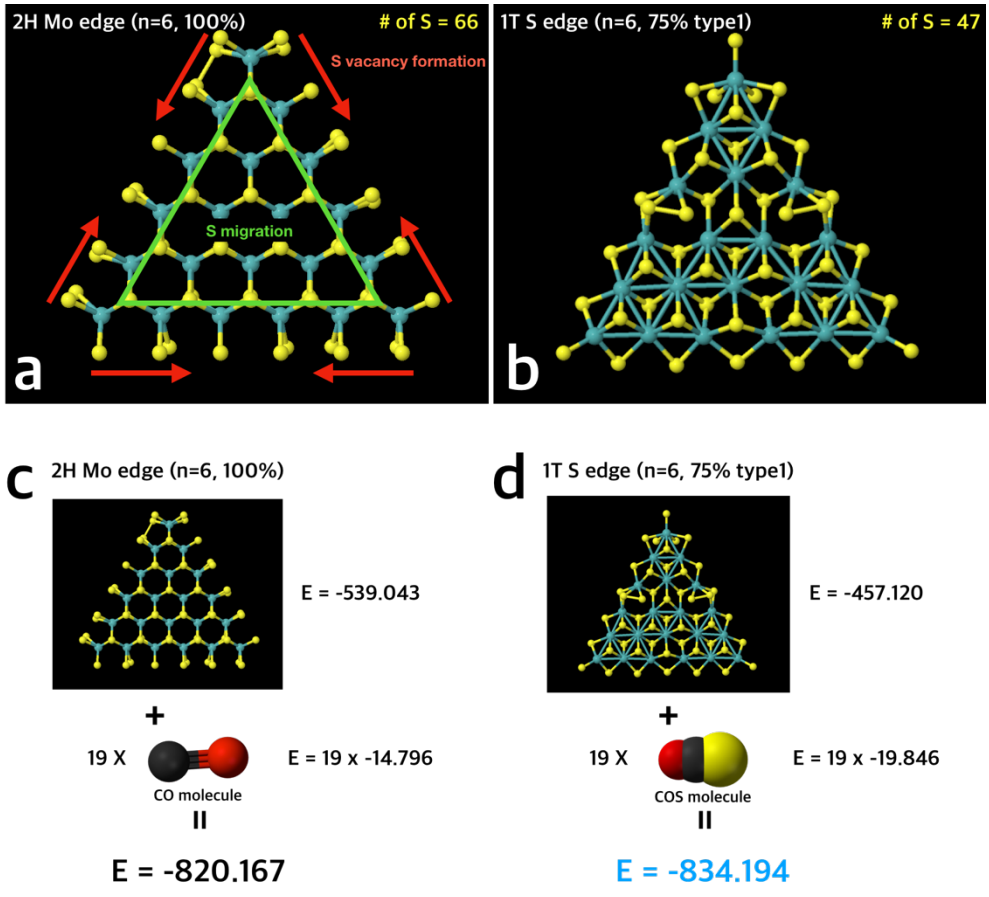

Figure 5.6. Explanation for the phase transition of the Mo edge nanocrystal. DFT optimized atomic model for a) 100% S coverage Mo edge 2H nanocrystal and b) type 1 75% S coverage S edge 1T nanocrystal (Size of both nanocrystals is n = 6). Total number of S atoms is 66 for Mo edge nanocrystal and 47 for S edge nanocrystal. c, d) Total energy estimation considering CO and COS molecules. After CO molecules are combined with the S atoms in the 2H Mo edge nanocrystal to form S vacancy and COS molecules, the total energy of the whole system lowered.

Total energy of the entire system can be compared assuming that the Mo edge nanocrystal is changed to the 1T phase nanocrystal (type 1 75% S coverage) shown in Figure 5.6.b. The 1T phase nanocrystal of Figure 5.6.b has 19 fewer S atoms than the Mo edge nanocrystal. In other words, 19 S atoms in the Mo edge nanocrystal should be desorbed by a CO molecule in order to transform to the 1T phase. Since the excess CO molecules that do not participate in the reaction have the same contribution to both total energies, it is only necessary to compare the energy of the CO molecules involved in the reaction, the COS molecules generated, and the MoS_2 nanocrystal. As shown in Figure 5.6.c and 5.6.d, total energy of the Mo edge nanocrystal plus 19 CO molecules is −802.167 eV and that of 1T phase nanocrystal with 19 COS molecules is −834.194 eV. From this result, it was confirmed that the transition of Mo edge nanocrystal to 1T phase is thermodynamically favorable reaction. Thus, in all cases that MoS_2 nanocrystals have S edge and Mo edge terminations, the transition to the 1T phase can be explained by the combination of the formation of S vacancies by CO molecules and the migration of S atoms on the surface.

5.4. Summary

We found that CO molecules can easily dissociate the S atoms at vertices and edges of the MoS_2 nanocrystals. After the S atoms at vertices and edges are dissociated, the S atoms on the surface that are covalently bonded to Mo atoms are easily migrated toward around S vacancy sites and the local arrangement of S atoms shifted from the trigonal prismatic symmetry to the octahedral (or partially distorted octahedral) symmetry, which is the crystallographic feature of 1T phase. Finally, the structure of the MoS_2 nanocrystal can be changed to the 1T phase. Surprisingly, it was found that the 1T phase MoS_2 nanocrystals with S deficient edge are thermodynamically more stable than the 2H phase. Through this, we were able to present a novel atomic-scale mechanism for a CO gas annealing method of phase engineering of MoS_2 nanocrystals and it will give guideline for making high-performance HER catalysts based on MoS_2 nanostructures.

5.5. Bibliography

[1] K. S. Novoselov, Science (80-.). **306**, 666 (2004).

[2] K. S. Novoselov, A. K. Geim, S. V Morozov, D. Jiang, M. I. Katsnelson, I. V. Grigorieva, S. V. Dubonos, and A. A. Firsov, Nature **438**, 197 (2005).

[3] K. H. Lee, H.-J. Shin, J. Lee, I. Lee, G.-H. Kim, J.-Y. Choi, and S.-W. Kim, Nano Lett. **12**, 714 (2012).

[4] Y. Shi, C. Hamsen, X. Jia, K. K. Kim, A. Reina, M. Hofmann, A. L. Hsu, K. Zhang, H. Li, Z.-Y. Juang, M. S. Dresselhaus, L.-J. Li, and J. Kong, Nano Lett. **10**, 4134 (2010).

[5] D. Pacile, J. C. Meyer, and C. O. Girit, Appl. Phys. Express (2008).

[6] G. CAMACHOBRAGADO, J. ELECHIGUERRA, A. OLIVAS, S. FUENTES, D. GALVAN, and M. YACAMAN, J. Catal. **234**, 182 (2005).

[7] H. S. S. R. Matte and A. Gomathi, Angew. Chemie Int. Ed. (2010).

[8] H. Zhou, F. Yu, Y. Liu, X. Zou, C. Cong, C. Qiu, T. Yu, Z. Yan, X. Shen, L. Sun, B. I. Yakobson, and J. M. Tour, Nano Res. **6**, 703 (2013).

[9] F. A. Rasmussen and K. S. Thygesen, J. Phys. Chem. C **119**, 13169 (2015).

[10] M. Osada and T. Sasaki, J. Mater. Chem. **19**, 2503 (2009).

[11] J. E. ten Elshof, H. Yuan, and P. Gonzalez Rodriguez, Adv. Energy Mater. **6**, 1600355 (2016).

[12] L. S. Byskov, J. K. Nørskov, B. S. Clausen, and H. Topsøe, J. Catal. **187**, 109 (1999).

[13] H. Shang, T. Wang, and W. Zhang, Chem. Eng. Sci. **195**, 208 (2019).

[14] J.-F. Paul and E. Payen, J. Phys. Chem. B **107**, 4057 (2003).

[15] A. Bruix, H. G. Füchtbauer, A. K. Tuxen, A. S. Walton, M. Andersen, S. Porsgaard, F. Besenbacher, B. Hammer, and J. V. Lauritsen, ACS Nano **9**, 9322 (2015).

[16] Q. Tang and D. Jiang, ACS Catal. **6**, 4953 (2016).

[17] B. Hinnemann, P. G. Moses, J. Bonde, K. P. Jørgensen, J. H. Nielsen, S. Horch, I. Chorkendorff, and J. K. Nørskov, J. Am. Chem. Soc. **127**, 5308 (2005).

[18] K. Chang, X. Hai, H. Pang, H. Zhang, L. Shi, G. Liu, H. Liu, G. Zhao, M. Li, and J. Ye, Adv. Mater. **28**, 10033 (2016).

[19] M. Acerce, D. Voiry, and M. Chhowalla, Nat. Nanotechnol. **10**, 313 (2015).

[20] M. A. Lukowski, A. S. Daniel, F. Meng, A. Forticaux, L. Li, and S. Jin, J. Am. Chem. Soc. **135**, 10274 (2013).

[21] A. N. Enyashin, L. Yadgarov, L. Houben, I. Popov, M. Weidenbach, R. Tenne, M. Bar-Sadan, and G. Seifert, J. Phys. Chem. C **115**, 24586 (2011).

[22] E. Scalise, M. Houssa, G. Pourtois, V. Afanas\textquoterightev, and A. Stesmans, Nano Res. **5**, 43 (2011).

[23] K. Q. Dang, J. P. Simpson, and D. E. Spearot, Scr. Mater. **76**, 41 (2014).

[24] Y.-C. Lin, D. O. Dumcenco, Y.-S. Huang, and K. Suenaga, Nat. Nanotechnol. **9**, 391 (2014).

[25] Y. Kang, S. Najmaei, Z. Liu, Y. Bao, Y. Wang, X. Zhu, N. J. Halas, P. Nordlander, P. M. Ajayan, J. Lou, and Z. Fang, Adv. Mater. **26**, 6467 (2014).

[26] A. N. Enyashin and G. Seifert, Comput. Theor. Chem. **999**, 13 (2012).

[27] M. Kan, J. Y. Wang, X. W. Li, S. H. Zhang, Y. W. Li, Y. Kawazoe, Q. Sun, and P. Jena, J. Phys. Chem. C **118**, 1515 (2014).

[28] G. Gao, Y. Jiao, F. Ma, Y. Jiao, E. Waclawik, and A. Du, J. Phys. Chem. C **119**, 13124 (2015).

[29] X. Sun, Z. Wang, Z. Li, and Y. Q. Fu, Sci. Rep. **6**, 26666 (2016).

[30] D.-H. Nam, H.-Y. Kang, J.-H. Jo, B. K. Kim, S. Na, U. Sim, I.-K. Ahn, K.-W. Yi, K. T. Nam, and Y.-C. Joo, Adv. Mater. **29**, 1605327 (2017).

[31] W. Zan, Z. Hu, Z. Zhang, and B. I. Yakobson, Nanoscale **8**, 19154 (2016).

[32] A. Bruix, J. V Lauritsen, and B. Hammer, (n.d.).

[33] J. V Lauritsen, J. Kibsgaard, S. Helveg, H. Topsøe, B. S. Clausen, E. Lægsgaard, and F. Besenbacher, Nat. Nanotechnol. **2**, 53 (2007).

[34] J. P. Perdew, K. Burke, and M. Ernzerhof, Phys. Rev. Lett. **77**, 3865 (1996).

[35] G. Kresse and J. Furthmuller, Phys. Rev. B **54**, 11169 (1996).

Chapter 6. Conclusion and perspective

In this dissertation, we investigated the effect of defects on the structural and electronic properties of 2D materials and proposed guidelines for novel applications of 2D materials. Graphene, which is the initiator of 2D materials research and MoS_2 were our mainly concerning host materials. We carried out first-principles calculation for defect engineering of these two materials and obtained the results as follows.

First topic of our study is related to electronic and magnetic properties of Fe-graphene system. We confirmed that interaction between Fe dopant pair in graphene lattice generates magnetic moment of 2 μ_B. In order to manipulate the interaction between Fe dopants, our approach was deforming graphene which has much larger size than atomic-size Fe dopant itself. Stretching and compressively outward bending graphene changed interaction between Fe dopants and magnetic moment was vanished dramatically. In this phenomenon, we verified that carbon atom adjacent to Fe dopants plays an important role that hindering interaction between Fe dopants.

Second topic of our study is related to stability and electronic properties of extrinsic defects in monolayer MoS_2. Cr and V dopants in MoS_2 were observed at Mo substitutional sites and we calculated formation energy considering its charge states. All the possible binary phases of Cr-S and V-S were also considered to explore different experimental scenarios. Cr_{Mo} is stable as electrically neutral and V_{Mo} is stable as neutral and -1 charged state. The (0/−1) transition level of V_{Mo} is 0.54 eV that indicates V_{Mo} acts as a single deep acceptor. Moreover, we found that neutral V_{Mo} shows local magnetic moment of 1 μ_B through the analysis of electronic density of states.

Last topic of our study is related to the role of defects in structural phase transition of triangular MoS_2 nanocrystals. We calculated reaction barriers for S

vacancy formation by CO molecules at the vertex, edge, and basal plane of MoS_2 nanocrystals. We found that S vacancy formation occurs more easily at the vertices and edges than at the basal plane. It was confirmed that S atoms in the basal plane migrate easily to space around S vacancy after the S vacancy was formed. We investigated that local structure of MoS_2 nanocrystal can be changed to 1T phase and this phase transition is thermodynamically favorable. Based on our results, we could suggest atomic-scale mechanism of phase transition of MoS_2 nanocrystals.

As a result, we could give guideline for novel applications through defect engineering of 2D materials. The result of Fe-graphene may help new opportunities to design systems that couple mechanical deformations with magnetism and find applications for novel nanoelectronic devices. We identified that Cr and V substitutional dopants are not useful to enhance electric conductivity of MoS_2. However, previous report supports that the dielectric environment can convert Cr and V dopants into useful dopants, and further study related to dielectric environment is needed. We also expect that atomic-scale mechanism of structural phase transition of MoS_2 nanocrystals can give advice for making high-efficient nanostructured HER catalysts which can alternate expensive noble-metal based conventional catalysts.

Defect engineering of 2D materials is a promising method because it improves the properties of materials, device performance, and exhibits unprecedented properties. However, there are many challenges in order to realize conventional applications of 2D materials via defect engineering. Techniques and tools such as high-resolution TEM, AFM, STM, and etc. that enable the manipulation and measurement of single atoms have been dramatically improved but intentional and rational control of defects is a difficult problem yet. Experimental settings such as ultra-high vacuum, low temperature, contamination free, atomic-scale manipulation and measurements are needed for advancing defect engineering of 2D materials. There has been a noticeable improvement in some areas and much effort is still being made.

Therefore, what can theoretical research contribute to the defect engineering of 2D materials? DFT calculations have been regarded as powerful tools for predicting the properties of materials. However, DFT calculations have limitations in describing the dynamic process which 2D materials are synthesized and defects are created, transformed, and vanished due to its computational cost. Molecular dynamics (MD) and kinetic Monte Carlo (kMC) method are to be expected as the potential candidates to unravel this limitation. MD and kMC also have their limitations but by developing a new method which can explore the creation and transformation of defects, it will be very helpful to experimental research of defect engineering of 2D materials.

국문 초록

2004년 그래핀이 처음 합성되었고 기존의 물질에서 찾아볼 수 없었던 뛰어난 특성들과 물리적 현상으로 인해 사람들의 많은 관심을 끌게 되었다. 이로부터 이차원 물질 연구라는 새로운 분야가 열리게 되었으며 그래핀 이외에도 전이금속 디칼코제나이드, 육방정계 질화붕소, 흑린 등의 다양한 이차원 물질들이 예측되고 합성되어지고 있다. 이차원 물질의 다양한 종류 만큼이나 그 응용분야도 다양하여 투명전극, 트랜지스터, 광검출소자, 배터리, 필터, 생명공학 등의 다양한 분야에서 연구가 이루어지고 있다. 그러나 이차원 물질이 기존에 사용되고 있는 물질을 대체하기에는 단결정/대면적 합성이라는 큰 장벽이 존재하고 있다. 이차원 물질의 합성 과정에서 생기는 결함은 이차원 물질의 뛰어난 특성들을 저하시켜 응용을 위한 효용성을 약화시킨다. 하지만 결함을 긍정적인 방향으로 잘 활용하면 이차원 물질의 특성을 향상시키거나, 기존에 없던 특성이나 현상을 발현 시킬 수 있다는 연구들도 보고되고 있다. 이러한 연구들을 통칭하여 이차원 물질의 결함 공학 이라고 부를 수 있으며, 본 논문에서는 밀도범함수 이론에 기반한 제일원리계산 기법을 사용하여 그래핀과 이황화몰리브덴에 존재하는 결함의 구조적, 전자적 특성에 대한 연구를 수행하였다.

첫째, 그래핀에 존재하는 철 원자 쌍의 상호작용이 그래핀의 변형에 따라 어떤 변화양상을 보이는지에 대한 연구를 수행하였다. 그래핀의 인접한 두개의 공공에 각각 철 원자가 공유 결합을 이루고 있을 때 두 철 원자간의 상호작용으로 인해 2 μ_B의 자기 모멘트가 생성되게 된다. 하지만 그래핀에 인장 변형을 가하거나, 압축 변형을 가하며 휘게 되면 철 원자간의 상호작용에 변화가 일어나 자기 모멘트가 급격히 사라지게

되는 현상을 발견하였다. 이 과정에서 두 개의 철 원자와 동시에 인접한 탄소 원자가 철 원자간의 상호작용을 방해하는 것을 확인하였으며 이에 대한 전자구조 분석을 수행하여 그 원리를 설명하였다.

둘째, 단일층 이황화몰리브덴의 몰리브덴 원자가 크롬과 바나듐 원자로 치환되어 있을 때 이에 대한 구조적 안정성과 전자적 성질에 대한 연구를 수행하였다. 이때 크롬과 바나듐 불순물이 가질 수 있는 전하 상태를 고려하였고 크롬과 바나듐 불순물이 생성될 때의 실험적 상황을 묘사하기 위해 크롬-황, 바나듐-황의 이원 상들을 고려하였다. 크롬은 전기적으로 중성을 띠며, 바나듐은 −1의 전하 상태와 중성 상태를 가질 수 있음을 확인하였고, 중성 상태의 바나듐 불순물은 1 μ_B의 국소적인 자기 모멘트를 가짐을 전자구조 분석을 통해 확인하였다.

셋째, 삼각형 형태의 이황화몰리브덴 나노결정이 황 공공의 생성으로 인해 구조적 상전이 현상을 일으키는 과정에 대한 연구를 수행하였다. 이황화몰리브덴 나노결정에 일산화탄소 기체를 통한 열처리를 가하게 되면 2H상에서 1T상으로 변화하는 최근 실험결과를 설명하기 위해 반응 장벽 에너지 계산을 수행하였다. 나노결정의 꼭지점과 모서리에 존재하는 황 원자들이 일산화탄소 분자에 의해 쉽게 탈착될 수 있음을 반응 장벽 에너지 계산을 통해 확인하였으며, 또한 황 공공이 생성되면서 생긴 빈 공간으로 나노결정의 기저면에 존재하는 황 원자들이 쉽게 이동하여 국부적인 구조가 1T상으로 변화하는 것을 확인하였다. 이를 통해 황 공공 생성과 황 원자 이동으로 설명되는 원자 수준의 상전이 기작을 제시할 수 있었다.

이상의 연구들을 통해 우리는 이차원 물질들을 대표하는 물질인 그래핀과 이황화몰리브덴에 존재하는 결함의 구조적, 전자적 성질에 대한 심도 있는 이해를 할 수 있었다. 또한 본 논문에서 제시된

결과들은 이차원 물질의 결함 공학을 통한 새로운 나노소자와 촉매 등의 개발에 대한 가이드라인이 될 수 있을 것으로 기대된다.

주요어: 이차원 물질, 그래핀, 이황화몰리브덴, 결함, 밀도범함수이론, 제일원리계산

학 번: 2014-30212

Publication list

1. **Sungwoo Lee**, Dongwook Kim, Alex W Robertson, Euijoon Yoon, Suklyun Hong, Jisoon Ihm, Jaejun Yu, Jamie H Warner, Gun-Do Lee. Graphene as a flexible template for controlling magnetic interactions between metal atoms. ***Journal of Physics: Condensed Matter*** (2017)
2. Dae-Hyun Nam*, **Sungwoo Lee***, Young-Joo Lee, Jun-Hyun Jo, Euijoon Yoon, Kyung-Woo Yi, Gun-Do Lee, Young-Chang Joo. Gaseous Nanocarving-Mediated Carbon Framework with Spontaneous Metal Assembly for Structure-Tunable Metal/Carbon Nanofibers. ***Advanced Materials*** (2017) **(*equal contribution)**
3. **Sungwoo Lee** *et al.* Atomic Scale Mechanism of MoS_2 Nanocrystals Structural Phase Transition from 2H to 1T using CO gas: DFT Calculations. (2019) **(In preparation)**
4. Hwanyeol Park, **Sungwoo Lee**, Ho Jun Kim, Daekwang Woo, Se Jun Park, Jong Myeong Lee, Euijoon Yoon, Gun-Do Lee. Effects of nitrogen doping in amorphous carbon layers on the diffusion of fluorine atoms: A first-principles study. ***Journal of Applied Physics*** (2019)
5. Hwanyeol Park, **Sungwoo Lee**, Ho Jun Kim, Daekwang Woo, Se Jun Park, Kangsoo Kim, Euijoon Yoon, Gun-Do Lee. Effects of H_2 and N_2 treatment for B_2H_6 dosing process on TiN surfaces during atomic layer deposition: an *ab initio* study. ***RSC Advances*** (2018)
6. Hwanyeol Park, **Sungwoo Lee**, Ho Jun Kim, Daekwang Woo, Jong Myeong Lee, Euijoon Yoon, Gun-Do Lee. Overall reaction mechanism for a full atomic layer deposition cycle of W films on TiN surfaces: First-principles study. ***RSC Advances*** (2018)
7. Hwanyeol Park, **Sungwoo Lee**, Ho Jun Kim, Euijoon Yoon, Gun-Do Lee. Dissociation reaction of B_2H_6 on TiN surfaces during atomic layer deposition:

first-principles study. ***RSC Advances*** (2017)

8. Chuncheng Gong, **Sungwoo Lee**, Suklyun Hong, Euijoon Yoon, Gun-Do Lee, Jamie H. Warner. Point Defects in Turbostratic Stacked Bilayer Graphene. ***Nanoscale*** (2017)
9. Ja Kyung Lee, Gun-Do Lee, **Sungwoo Lee**, Euijoon Yoon, Harry L. Anderson, G. Andrew D. Briggs, Jamie H. Warner. Atomic Scale Imaging of Reversible Ring Cyclization in Graphene Nanoconstrictions. ***ACS Nano*** (2019)
10. Ji-Yong Kim, Hwanyeol Park, Wonhyo Joo, Dae-Hyun Nam, **Sungwoo Lee**, Hyoung Gyun Kim, In-Kyoung Ahn, Ho-Young Kang, Gi-Baek Lee, In-Ho Jung, Miyoung Kim, Gun-Do Lee, Young-Chang Joo. Predictive Fabrication of Ni Phosphide Embedded in Carbon Nanofibers as Active and Stable Electrocatalysts. ***Journal of Materials Chemistry A*** (2019)
11. Se-Yang Kim, Jung Hwa Kim, **Sungwoo Lee**, Jinsung Kwak, Yongsu Jo, Euijoon Yoon, Gun-Do Lee, Zonghoon Lee, Soon-Yong Kwon. The Impact of Substrate Surface Defects on the Properties of Two-Dimensional van der Waals Heterostructures. ***Nanoscale*** (2018)
12. Jinsung Kwak, Yongsu Jo, Seunguk Song, Jung Hwa Kim, Se-Yang Kim, Jae-Ung Lee, **Sungwoo Lee**, Jungmin Park, Kangwon Kim, Gun-Do Lee, Jung-Woo Yoo, Sung Youb Kim, Young-Min Kong, Gwan-Hyoung Lee, Wan-Gyu Lee, Jucheol Park, Xiaodong Xu, Hyeonsik Cheong, Euijoon Yoon, Zonghoon Lee, Soon-Yong Kwon. Single-Crystalline Nanobelts Composed of Transition Metal Ditellurides. ***Advanced Materials*** (2018)
13. Min Sup Choi, Byung-ki Cheong, Chang Ho Ra, Suyoun Lee, Jee-Hwan Bae, **Sungwoo Lee**, Gun-Do Lee, Cheol-Woong Yang, James Hone, Won Jong Yoo. Electrically Driven Reversible Phase Changes in Layered In_2Se_3 Crystalline Film. ***Advanced Materials*** (2017)
14. Alex W Robertson, Yung-Chang Lin, Shanshan Wang, Hidetaka Sawada, Christopher S Allen, Qu Chen, **Sungwoo Lee**, Gun-Do Lee, Joohee Lee,

Seungwu Han, Euijoon Yoon, Angus I Kirkland, Heeyeon Kim, Kazu Suenaga, Jamie H Warner. Atomic Structure and Spectroscopy of Single Metal (Cr, V) Substitutional Dopants in Monolayer MoS_2. ***ACS Nano*** (2016)

15. Shanshan Wang, Gun-Do Lee, **Sungwoo Lee**, Euijoon Yoon, Jamie H Warner. Detailed Atomic Reconstruction of Extended Line Defects in Monolayer MoS_2. ***ACS Nano*** (2016)
16. Baeckkyoung Sung, Se Hoon Kim, **Sungwoo Lee**, Jaekwan Lim, Jin-Kyu Lee, Kwang-Sup Soh. Nanofluid transport in a living soft microtube. ***Journal of Physics D: Applied Physics*** (2015)
17. Alex W Robertson, Gun-Do Lee, Kuang He, Ye Fan, Christopher S Allen, **Sungwoo Lee**, Heeyeon Kim, Euijoon Yoon, Haimei Zheng, Angus I Kirkland, Jamie H Warner. Partial Dislocations in Graphene and Their Atomic Level Migration Dynamics. ***Nano Letters*** (2015)
18. Qu Chen, Ai Leen Koh, Alex W Robertson, Kuang He, **Sungwoo Lee**, Euijoon Yoon, Gun-Do Lee, Robert Sinclair, Jamie H Warner. Rotating Anisotropic Crystalline Silicon Nanoclusters in Graphene. ***ACS Nano*** (2015)
19. Kuang He, Alex W Robertson, **Sungwoo Lee**, Euijoon Yoon, Gun-Do Lee, Jamie H Warne. Extended Klein Edges in Graphene. ***ACS Nano*** (2014)